

This is a pre-copyedited, author-produced PDF of an article accepted for publication in *Geophys. J. Int.* following peer review. The version of record “Takemura, S., Okuwaki, R., Kubota, T., Shiomi, K., Kimura, T., & Noda, A., Centroid moment tensor inversions of offshore earthquakes using a three-dimensional velocity structure model: slip distributions on the plate boundary along the Nankai Trough” is available online at <https://doi.org/10.1093/gji/ggaa238>.
https://academic.oup.com/journals/pages/self_archiving_policy_p

1
2
3
4
5
6
7
8
9
10
11
12
13
14
15
16
17
18
19
20
21
22
23
24
25
26
27
28

Centroid moment tensor inversions of offshore earthquakes using a three-dimensional velocity structure model: Slip distributions on the plate boundary along the Nankai Trough

Authors

**Shunsuke TAKEMURA^{1*}, Ryo OKUWAKI², Tatsuya KUBOTA³, Katsuhiko SHIOMI³
Takeshi KIMURA³, Akemi NODA⁴**

¹Earthquake Research Institute, the University of Tokyo, 1-1-1 Yayoi, Bunkyo-ku, Tokyo, 113-0032, Japan

² Mountain Science Center, Faculty of Life and Environmental Sciences, University of Tsukuba, 1-1-1 Tennodai, Tsukuba 305-8572, Japan.

³Network Center for Earthquake, Tsunami and Volcano, National Research Institute for Earth Science and Disaster Resilience, 3-1 Tennodai, Tsukuba, Ibaraki, 305-0006, Japan.

⁴Earthquake and Tsunami Research Division, National Research Institute for Earth Science and Disaster Resilience, 3-1 Tennodai, Tsukuba, Ibaraki, 305-0006, Japan.

Running Title

3D CMT inversion along the Nankai Trough

Corresponding Author

Shunsuke Takemura

E-mail: shunsuke@eri.u-tokyo.ac.jp

Phone: +81 3-5841-5689

29 **Summary**

30 Due to complex three-dimensional (3D) heterogeneous structures, conventional one-
31 dimensional (1D) analysis techniques using onshore seismograms can yield incorrect
32 estimation of earthquake source parameters, especially dip angles and centroid depths of
33 offshore earthquakes. Combining long-term onshore seismic observations and numerical
34 simulations of seismic wave propagation in a 3D model, we conducted centroid moment
35 tensor (CMT) inversions of earthquakes along the Nankai Trough between April 2004 and
36 August 2019 to evaluate decade-scale seismicity. Green's functions for CMT inversions of
37 earthquakes with moment magnitudes of 4.3–6.5 were evaluated using finite-difference
38 method simulations of seismic wave propagation in the regional 3D velocity structure model.
39 Significant differences of focal mechanisms and centroid depths between previous 1D and
40 our 3D catalogues were found in the solutions of offshore earthquakes. By introducing the 3D
41 structures of the low-velocity accretionary prism and the Philippine Sea Plate, dip angles and
42 centroid depths for offshore earthquakes were well-constrained. Teleseismic CMT also
43 provides robust solutions, but our regional 3D CMT could provide better constraints of dip
44 angles. Our 3D CMT catalogue and published slow earthquake catalogues depicted spatial
45 distributions of slip behaviours on the plate boundary along the Nankai Trough. The regular
46 and slow interplate earthquakes were separately distributed, with these distributions reflecting
47 the heterogeneous distribution of effective strengths along the Nankai Trough plate boundary.
48 By comparing the spatial distribution of seismic slip on the plate boundary with the slip-
49 deficit rate distribution, regions with strong coupling were clearly identified.

50

51 **Keywords:**

52 Computational seismology, earthquake ground motions, earthquake source observations,
53 seismicity and tectonics, wave propagation

54

55 1. Introduction

56 Focal mechanisms of earthquakes and their spatial distributions are important for
57 evaluating tectonic/local stress and strain fields (e.g. Saito *et al.* 2018, Terakawa & Matsu'ura
58 2010, Townend & Zoback 2006). To determine focal mechanisms, first-*P* or *S* polarisation
59 inversion (e.g. Hardebeck & Shearer 2002, Shelly *et al.* 2016) and waveform-based centroid
60 moment tensor (CMT) inversion (e.g. Dziewonski *et al.* 1981, Ekström *et al.* 2012, Kanamori
61 & Rivera 2008) techniques have been widely used around the world. One-dimensional (1D)
62 Earth models are assumed in typical focal mechanism determination methods. In regions with
63 complex three-dimensional (3D) heterogeneous structures, first-motion solutions using the
64 1D Earth model systematically show mis-estimations (e.g. Takemura *et al.* 2016). Although
65 CMT methods based on long-period (> 10 s) waveforms can be applied only for moderate-to-
66 large earthquakes due to signal-to-noise problems for long-period components, their
67 evaluations of source parameters are generally robust against structural heterogeneities in
68 comparison to first-motion solutions.

69 Along the Nankai Trough, megathrust earthquakes have repeatedly occurred at intervals of
70 100–150 years (e.g. Ando 1975). Evaluating seismicity around this region is important for
71 contributing to the understanding of megathrust earthquakes, such as evaluating stress
72 accumulation/release processes on plate boundaries. In Japan, regular and slow earthquakes
73 have been systematically monitored by the seismic networks of the Monitoring of Waves on
74 Land and Seafloor (MOWLAS; <https://doi.org/10.17598/NIED.0009>) operated by the
75 National Research Institute for Earth Science and Disaster Resilience (NIED; Okada *et al.*
76 2004). According to the combined earthquake catalogues of the International Seismological
77 Centre-Global Earthquake Model (ISC-GEM; Storchak *et al.* 2013), the Japan Meteorological
78 Agency (JMA), and the NIED F-net (Fukuyama *et al.* 1998, Kubo *et al.* 2002), the seismicity
79 of regular earthquakes along the Nankai Trough, especially interplate earthquakes, is quite
80 low. Figure 1 shows the spatial distribution of regular earthquakes with moment magnitudes
81 (M_w) of 4.3–6.5 that occurred from April 2004 to August 2019, as listed in the F-net moment
82 tensor (F-net MT) catalogue. The regional moment tensor inversion can be applied to
83 earthquakes with $M_w >$ about 4, which is smaller than a lower limit of teleseismic moment
84 tensor inversion (e.g., Figure 5 of Ekström *et al.* 2012). This is an advantage for discussing
85 detail seismicity in a certain region. A few shallow offshore earthquakes occurred in the
86 Tonankai and Nankai regions, and their focal mechanisms in the F-net catalogue were not
87 characterised by low-angle thrust faulting. In other words, no earthquakes suggesting faulting

88 on the plate boundary around the Tonankai and Nankai regions are listed in the F-net MT
89 catalogue.

90 On 1 April 2016, the M_w 5.8 earthquake, called “2016 southeast off the Kii Peninsula
91 earthquake”, occurred in the Tonankai region (marked A in Figure 1). The F-net MT solution
92 of this earthquake was characterised by high-angle (38°) reverse faulting below the upper
93 surface of the Philippine Sea Plate, indicating it was an intraslab earthquake. However, a
94 detailed analysis of this earthquake revealed that it could be modelled by low-angle thrust
95 faulting at a depth of approximately 10 km, suggesting seismic slip along the plate boundary
96 (e.g. Nakano *et al.* 2018a, Takemura *et al.* 2018a, Wallace *et al.* 2016). Source models
97 suggested in these studies were also consistent with a model based on observed tsunami data
98 (Kubota *et al.* 2018). In regions with a thick accretionary prism, characteristics of surface
99 wave propagation are significantly affected by a low-velocity accretionary prism (e.g.
100 Gomberg 2018, Kaneko *et al.* 2019, Shapiro *et al.* 1998). Thus, the focal mechanisms of other
101 offshore earthquakes along the Nankai Trough could be incorrectly estimated using
102 conventional 1D regional MT inversion, even for long-period displacements. Indeed, shallow
103 very low frequency earthquakes along the Nankai Trough have been interpreted as low-angle
104 thrust faulting on the plate boundary by using offshore seismic observations (e.g. Nakano *et al.*
105 *et al.* 2018b), but their focal mechanisms based on 1D analysis of onshore observations were
106 high-angle reverse faulting mechanisms within the accretionary prism (e.g., Ito & Obara
107 2006). To evaluate seismic activity along the Nankai Trough more precisely, offshore
108 earthquakes listed in the previous 1D catalogues require re-analysis.

109 Parallel simulation codes of seismic wave propagation (e.g. Gokhberg & Fichtner 2016,
110 Maeda *et al.* 2017) and 3D seismic velocity structure models (e.g. Eberhart-Phillips *et al.*
111 2010, Koketsu *et al.* 2012) enable the simulation of Green’s functions propagating through
112 realistic 3D Earth models (hereafter called ‘3D Green’s functions’), which have been used to
113 develop CMT inversions (e.g. Hejrani *et al.* 2017, Lee *et al.* 2013, Okamoto *et al.* 2018,
114 Ramos-Martínez & McMechan 2001, Takemura, *et al.* 2018ab, 2019, Wang & Zhan 2020).
115 Although the resolution of detailed source characteristics for offshore earthquakes derived
116 using the 3D CMT method and onshore seismograms is limited compared to those using
117 offshore observations, these methods provide similar focal mechanisms and centroid
118 locations (see Figure 2 of Takemura *et al.* 2018b). Thus, offshore seismic activity, including
119 earthquakes before offshore seismic observations, can be effectively evaluated.

120 To investigate the decade-scale seismicity of offshore earthquakes along the Nankai

121 Trough, we re-evaluated focal mechanisms based on CMT inversion using 3D Green's
122 function datasets, which were evaluated by numerical simulations of seismic wave
123 propagation in a regional 3D velocity structure model. Then, to investigate spatial variation in
124 slip behaviours on the plate boundary along the Nankai Trough, we compared the spatial
125 distribution of focal mechanisms based on the 3D CMT technique with the spatial
126 distribution of slip-deficit rates (Noda *et al.* 2018), slow slip events (SSEs; Kobayashi 2014,
127 Miyazaki *et al.* 2006, Nishimura *et al.* 2013, Takagi *et al.* 2016, 2019, Yokota & Ishikawa
128 2020), shallow low-frequency tremors (LFTs; Yamashita *et al.* 2015), shallow very low-
129 frequency earthquakes (VLFEs; Takemura *et al.* 2019b), and the 1968 Hyuga-nada
130 earthquake (Yagi *et al.* 1998).

131

132 **2. Data and Methods**

133 We used three-component (NS, EW, and UD) velocity seismograms from F-net (NIED
134 2019), for which the performance of the sensors have been systematically monitored (Kimura
135 *et al.* 2015). To conduct CMT inversion of the target earthquakes, we applied a band-pass
136 filter with passed periods of 25–100 s. We selected a 25–100 s period band because ground
137 motions for periods of 8–20 s are significantly affected by internal structures of the
138 accretionary prism along the Nankai Trough (e.g. Takemura *et al.* 2019a). The selected period
139 band is enough longer than corner periods of source spectra for target earthquakes. In our
140 CMT inversions, we used 10-min F-net velocity seismograms from three minutes before the
141 initial origin minute to conduct pre-processing (filter and integration) stably. We obtained
142 displacement waveforms by calculating time integration of each filtered velocity record. The
143 target earthquakes occurred within the region of assumed source grids (grey crosses in Figure
144 2) between April 2004 and August 2019, and values of M_w in the F-net catalogue ranging
145 from 4.3 to 6.5. According to the signal-to-noise ratios for the target period band, the
146 magnitude range of the analysed earthquake was determined by trial and error. Source grids
147 were uniformly distributed at horizontal intervals of 0.1° . Depths of source grids ranged from
148 6 to 50 km at an interval of 2 km. The total number of source grids was 61,433.

149 Green's functions were evaluated by solving equations of motion in the 3D viscoelastic
150 medium model based on the finite-difference method (FDM) simulations. The 3D simulation
151 model covered an area of $900 \times 1,000 \times 100 \text{ km}^3$, which was discretised by grid intervals of
152 0.5 km in the horizontal direction and 0.2 km in the vertical direction. We used a parallel
153 simulation code of OpenSWPC (Maeda *et al.* 2017), which includes the reciprocal calculation

154 mode for effectively evaluating Green's functions. The reciprocal calculation has proved very
155 useful in the case that the number of seismic source grids is significantly larger than the
156 number of seismic stations (e.g. Eisner & Clayton 2001, Hejrani *et al.* 2017, Okamoto *et al.*
157 2018). We obtained a total of approximately 35,000,000 Green's function SAC files from
158 61,433 source grids to 32 F-net stations (black and blue filled triangles in Figure 2) via 96
159 reciprocal FDM calculations. The source time function of each Green's function was the
160 K pper wavelet with a duration of 1 s.

161 The 3D velocity model of Koketsu *et al.* (2012) was used, as it has been widely applied in
162 studies of seismic ground motions across Japan. The configurations of the subducting oceanic
163 plate and the Moho discontinuity are consistent with other models (e.g., Hirose *et al.* 2008,
164 Shiomi *et al.* 2006). The oceanic crust of the model of Koketsu *et al.* (2012) has
165 approximately 7 km thickness, which corresponds to those by seismic surveys (e.g.,
166 Nakanishi *et al.* 2002). The topography model in our simulations was the ETOPO1 model
167 (Amante & Eakins 2009). The P - and S -wave velocities and density (V_P , V_S and ρ) in the
168 seawater layer were 1.5 km/s, 0.0 km/s and 1.04 g/cm³, respectively. The air column was
169 modelled as a vacuum with V_P of 0.0 km/s, V_S of 0.0 km/s and ρ of 0.001 g/cm³. The
170 minimum V_S in the solid column of 1.5 km/s was assumed. The accretionary prism is
171 important for constraining centroid depth, but detail velocity structure within the accretionary
172 prism has limited effects on long-period (> 20 s) seismograms (Figures 5 and 6 of Takemura
173 *et al.* 2019a).

174 Simulations were conducted using the computer system of the Earthquake and Volcano
175 Information Center at the Earthquake Research Institute, the University of Tokyo. Each
176 simulation required 385 GBytes of computer memory and a wall-clock time of 2.5 hours and
177 was performed using parallel computing with 432 cores to evaluate seismic wave propagation
178 of 200 s with 20,000 time-step calculations. According to our grid and model settings, our
179 FDM simulation can precisely evaluate long-period (> 10 s) seismic wave propagation.

180 Examples of Green's functions are illustrated in the right panels of Figure 2. The source
181 (red star) was located at a depth of 10 km, near the plate boundary. We employed the
182 Cartesian coordinate system of Aki & Richards (2002), where x , y , and z are taken as north,
183 east, and down, respectively. Due to the low-velocity accretionary prism and seawater,
184 durations of surface waves were amplified and elongated. In particular, for $M_{xy} = 1.0$ (i.e. a
185 pure strike-slip with strike angle of 0°, dip angle of 90°, and rake angle of 0°), Love waves on
186 horizontal components were strong and long. We assumed six-element moment tensors for

187 the CMT inversions, which includes five double couple and isotropic moment tensors (e.g.
188 Kikuchi & Kanamori 1991).

189 In the CMT inversions, we basically used Green's functions at F-net stations within
190 epicentral distances of 100–400 km from the initial epicentre. The initial epicentre was
191 obtained from the F-net MT catalogue. In cases where earthquake $M_w < 4.5$, we selected a
192 distance range of 100–350 km due to the signal-to-noise ratio of the observed waveforms for
193 the analysed period. We visually checked the filtered displacement waveforms and discarded
194 noisy ones. Centroid location and time of the analysed earthquake were determined using grid
195 search inversion. Because the analysis period range was longer than the source durations of
196 target earthquakes with $M_w = 4.3–6.5$, we did not estimate source durations of these events. A
197 set of Green's functions at the source grids, which were located in a $\pm 0.4^\circ$ region from the
198 initial epicentre and were distributed at depths of 6–50 km, was selected for the grid search
199 inversion.

200 The CMT inversions were conducted for each selected source grid every 1 s from three
201 minutes before the origin minute as recorded in the F-net catalogue. We used a 200-s time
202 window for each CMT inversion. During grid search CMT inversion, we did not allow time
203 shifts between synthetic and observed seismograms. After CMT inversion at all of the
204 selected source grids, we obtained seismic moments and focal mechanisms at all locations
205 and times. To identify the optimal solution, we evaluated variance reductions (VRs) between
206 the observed and synthetic displacement seismograms for periods of 25–100 s. The VR
207 could then be evaluated using the following equation:

$$VR = \left[1 - \frac{\sum_{i=1}^{N_S} \int (u_i^{Obs.}(t) - u_i^{Syn.}(t))^2 dt}{\sum_{i=1}^{N_S} \int (u_i^{Obs.}(t))^2 dt} \right] \times 100 [\%] \quad (1)$$

208 where N_S is the number of stations and $u_i^{Obs.}$ and $u_i^{Syn.}$ are the time-series of observed and
209 synthetic displacements, respectively. If observed and synthetic seismograms are perfectly
210 matched, VR is 100 %. The solution with the maximum VR was considered the optimal
211 solution, providing the optimal centroid location, depth, time, focal mechanism, and seismic
212 moment of each earthquake. In the case that the optimal solution was located at the edges of
213 the initial source grids, we performed the CMT inversion again using Green's functions for a
214 broader source grid dataset. In the cases of regions around the edges of all source grids (all
215 crosses in Figure 2), such as southern Kyushu and eastern Izu, we could not extend the grid
216 set, and then the optimal solution was located at the grid edge. These events may include
217 possibilities of some shifts outside the edges of the assumed source grids. Our grid search

218 CMT inversion required approximately 15–20 minutes using a typical, single-core desktop
219 machine.

220

221 **3. Results**

222 We obtained a total of 215 CMT solutions for moderate earthquakes that occurred between
223 April 2004 and August 2019. We discarded the solutions with a maximum VR of less than
224 20%. Our 3D CMT catalogue is listed in Global CMT (GCMT) format in the Supplementary
225 data (Table S1) and the CSV format full catalogue data is available from
226 <https://doi.org/10.5281/zenodo.3674161>. The size distribution and magnitude-time diagram
227 of our 3D CMT catalogue are shown in Figures S1 and S2. The estimated moment
228 magnitudes were slightly changed from the original F-net catalogue. The VRs of earthquakes
229 with small magnitudes tended to be low (Figure S2) due to the signal-to-noise ratio for the
230 analysed period range. We also compared our results with the GCMT catalogue (Figure S1).
231 Teleseismic CMT inversion is robust, but our regional CMT catalogue contains more
232 earthquakes, whose M_w values are less than about 5.

233 Figures 3 and 4 show examples of CMT solutions for the southeast off the Kii Peninsula
234 earthquake (1 April 2016) and the Hyuga-nada earthquake (9 May 2019), respectively. In our
235 previous study (Takemura *et al.* 2018a), the 2016 southeast off the Kii Peninsula earthquake
236 was also analysed. The epicentre location and origin time were fixed in the previous study.
237 We re-analysed this earthquake via full 3D CMT inversion, which estimates centroid
238 location, depth, time, and moment tensor. The F-net MT solution of this earthquake was a
239 high-angle (38°) reverse faulting mechanism (grey focal sphere in Figure 3). Its optimal
240 solution is an M_w 5.9 low-angle (10°) thrust faulting at a depth of 10 km (Figure 3), which is
241 close to the plate boundary (e.g. Kamei *et al.*, 2012; Park *et al.*, 2010). The synthetic
242 seismograms of the optimal solution corresponded well with the observations. The depth
243 variation of VRs illustrated a clear peak around the optimal depth. The centroid depth of this
244 earthquake was well constrained by our CMT inversion. Takemura *et al.* (2018a) numerically
245 demonstrated that the low-velocity accretionary prism just above the seismic source—which
246 controls long-period surface wave propagation—provides a better constraint on the centroid
247 depth. They also demonstrated that the 3D oceanic plate has an important role in constraining
248 focal mechanism (Figures 7 and 8 of Takemura *et al.* 2018a).

249 The centroid location was also close to that estimated by ocean-bottom seismometers
250 deployed just above the source region (Nakano *et al.* 2018a, Wallace *et al.* 2016), while the

251 GCMT solution was slightly (0.2°) shifted to the south (Figure S3). The CMT result was
252 consistent with models estimated by offshore observations (Kubota *et al.* 2018, Nakano *et al.*
253 2018a, Wallace *et al.* 2016). Especially, by using travel times, tsunami, and afterslip records,
254 Wallace *et al.* (2016) and Nakano *et al.* (2018a) concluded that this earthquake could be
255 interpreted as an interplate earthquake. Our CMT solution based on 3D Green's functions and
256 onshore seismograms also suggests this earthquake was due to faulting on the plate boundary.

257 Figure 4 shows the results of the CMT inversion and waveform fitting for the Hyuga-nada
258 earthquake on 9 May 2019. The F-net MT solution was also high-angle (33°) reverse faulting.
259 The optimal CMT solution indicated an M_w 6.2 low-angle (16°) thrust mechanism. The dip
260 angle from the CMT solution agreed well with that of the Philippine Sea Plate around this
261 earthquake. The synthetic waveforms also corresponded well to observed ones. Although the
262 optimal depth (26 km) was determined to be close to the upper surface of the Philippine Sea
263 Plate (approximately 27 km), a high VR ($> 80\%$) area was found within a wider depth range
264 (16–32 km). Because the depth of this earthquake was deeper than the 2016 southeast off the
265 Kii Peninsula earthquake, the effects of the low-velocity accretionary prism might not have
266 been so strong. Thus, the depth resolution of the CMT solutions might not be good when
267 compared to the case of the 2016 southeast off the Kii Peninsula earthquake. To constrain the
268 hypocentre depth more sharply, additional data, such as shorter-period (~ 4 s) first-arrival P -
269 wave waveforms, would need to be considered (e.g. Okamoto *et al.* 2018, Takemura *et al.*
270 2018a, Wang & Zhan 2020).

271 Figure 5 shows a comparison of the estimated focal mechanisms for the F-net and our 3D
272 CMT catalogues. Our CMT solutions of onshore earthquakes did not differ significantly from
273 the F-net solutions. However, our offshore CMT solutions differ from those based on the F-
274 net 1D analysis. In particular, dip angles and centroid depths of offshore earthquakes—which
275 are important for distinguishing interplate and intraslab earthquakes—were different.
276 Differences in dip angles and depths were clearly illustrated in detailed comparisons of
277 seismicity southeast off the Kii Peninsula and the Hyuga-nada (Figures 6, 7, S4, and S5). The
278 conventional 1D CMT inversion poorly estimated the dip angles of offshore earthquakes that
279 occurred outside of onshore seismic arrays due to the lack of the 3D subducting oceanic plate
280 and the accretionary prism (e.g. Takemura *et al.* 2018ab). The comparisons and error
281 estimations of dip angles are illustrated in Figures 9 and 10. The comparison of spatial
282 distributions of CMT solutions with the GCMT catalogue is also illustrated in Figure S3.

283 We focused our attention on seismicity southeast off the Kii Peninsula and the Hyuga-nada

284 (local names are illustrated in Figure 1), where seismic activities are relatively high in the
285 Nankai subduction zone. Figure 6 shows spatial distributions of the CMT solutions southeast
286 off the Kii Peninsula. We also plotted shallow VLFs in the catalogue of Takemura *et al.*
287 (2019b) as grey focal spheres. Shallow VLFs, which were characterised by low-angle thrust
288 faulting, were concentrated near the trench. In the region with shallow VLFE active, low-
289 angle thrust type CMT solution at depths of 5-10 km, which suggests seismic slip on the plate
290 boundary, was not estimated. On the down-dip side of the shallow VLFE region, a low-angle
291 thrust faulting mechanism was estimated at a depth near the plate boundary (along with
292 profile A in Figure 6). This earthquake is the 2016 southeast off the Kii Peninsula earthquake
293 (Figure 3). Almost all of the other earthquakes plotted in Figure 6 are aftershocks of the 2004
294 *Mw* 7.5 intraslab earthquake that occurred on 5 September 2004 southeast off the Kii
295 Peninsula. Our CMT solutions of these aftershocks were separately distributed at two depths
296 within the oceanic crust and mantle (10–15 and 20–30 km depths). This separation
297 corresponded well to the hypocentre depth distributions of the aftershocks of the *Mw* 7.5
298 earthquake as determined using ocean-bottom seismometers (e.g., Nakano *et al.* 2015, Sakai
299 *et al.* 2005). On the other hand, almost all the centroid depths of the F-net solutions were
300 concentrated within the accretionary prism, crust and oceanic crust (5–15 km depths; Figure
301 S3). According to comparisons with the detail hypocentre distributions in this region, even
302 for earthquakes near the trough axis, our CMT method provided better constraints for
303 centroid depths, compared to the 1D F-net MT solutions.

304 Figure 7 shows the spatial distribution of CMT solutions around the Hyuga-nada region.
305 Our CMT solutions characterised by low-angle thrust faulting mechanisms were distributed
306 across the region with average slip rates of approximately 20–40 mm/yr as inferred from
307 small repeating earthquakes (e.g., Yamashita *et al.* 2012). The optimal centroid depths of such
308 thrust solutions were concentrated around the plate boundary (profiles B and C in Figure 7).
309 The distribution of our CMT solutions agreed with that derived from onshore and temporal
310 offshore seismometers (Tahara *et al.* 2008). The 3D CMT solutions, especially for depths and
311 low-angle thrust faulting mechanisms, corresponded to the areas of detected repeating
312 earthquakes (Yamashita *et al.* 2012). Our 3D CMT also worked well in this region. The dip
313 angles of the F-net MT solutions at depths around the plate boundary were slightly higher
314 than those of the plate boundary, as shown in Figure S4. The centroid depths of the F-net
315 catalogue were also slightly deeper than the depths of the plate boundary. These also might
316 have been due to a lack of 3D geometry of the subducting oceanic plate in the 1D analysis.

317 To evaluate differences between 3D CMT and F-net MT solutions, we calculated
318 correlation coefficients of *P*-wave radiation patterns (e.g., Helffrich 1997, Kuge &
319 Kawakatsu 1993) between two catalogues. We also calculated differences of estimated
320 centroid depths from corresponding F-net solutions. Figure 8 shows the spatial distribution of
321 correlation coefficients of *P*-wave radiation patterns and depth differences between our CMT
322 and F-net MT catalogues. The values of correlation coefficients of offshore earthquakes
323 (enclosed by dashed lines in Figure 8a) were widely distributed. Centroid depths of offshore
324 earthquakes were also different from those of the F-net catalogue. Other earthquakes, which
325 occurred in onshore regions or had good station coverages, have high similarities and small
326 depth differences. The rigidity of the 3D model complicatedly depends on the centroid
327 location, and consequently, depth shifts could cause shifts of moment magnitudes from the F-
328 net catalogue (Figure S1). We also plotted comparisons of estimated depths with
329 corresponding GCMT solutions in Figure 3c. Almost of our centroid depths were 0-5 km
330 shallower than those in the GCMT catalogue.

331 The parameter of the dip angle is important for distinguishing earthquake types. In the
332 Nankai subduction zone, because megathrust earthquakes have repeatedly occurred,
333 seismicity of interplate earthquakes is important. We selected low-angle thrust faulting
334 solutions at depths around the plate boundary from our 3D CMT catalogue. These selected
335 events could be interpreted as seismic slips on the plate boundary. Figure 9 shows a
336 comparison of dip angles between the Philippine Sea plate and suggestive interplate
337 earthquakes from the 3D CMT catalogue. We also compared dip angles of corresponding
338 earthquakes in the F-net MT and GCMT catalogues. Although dip angles of F-net catalogues
339 were higher angles compared to the Philippine Sea plate, our CMT solutions well correlated
340 with dip angles of the plate boundary. Dip angles of the GCMT catalogue roughly
341 corresponded to dip angles of the Philippine Sea plate, but our solutions showed better
342 agreements with the plate dip angles. The teleseismic CMT solutions are generally robust, but
343 regional 3D CMT could provide better constraints of dip angles.

344 We also calculated the VRs between observed and synthetic displacement waveforms to
345 discuss estimation errors of dip angles for offshore earthquakes. Synthetic displacement
346 waveforms were calculated from 3D Green's functions, assuming double-couple point
347 sources and fixing hypocentre locations and seismic moments. Figure 10 shows spatial
348 distributions of VRs for the 2016 southeast off Kii Peninsula earthquake and the 2019 Hyuga-
349 nada earthquake. Clear trade-offs between strike and rake angles appeared in the strike-rake

350 plane (upper panels). We confirmed that higher VR values ($> 75\%$) only appeared in the
351 regions with dip angles of $5\text{-}15^\circ$ and $10\text{-}20^\circ$ for both earthquakes. Thus, our 3D CMT
352 provides constraints of dip angles with uncertainties of approximately $\pm 5^\circ$.

353

354 **4. Discussion**

355 **4.1. Slip behaviours on the plate boundary along the Nankai Trough**

356 In order to discuss slip behaviour on the plate boundary, Figure 11 shows the spatial
357 distribution of slow earthquakes and earthquakes with low-angle ($< 25^\circ$) thrust faulting
358 solutions at depths around the plate boundary along the Nankai Trough. The large coseismic
359 slip area of the 1968 $M_w 7.5$ earthquake (Yagi *et al.* 1998) is indicated by the blue area in
360 Figure 11. The cumulative deep SSE slips in each grid were determined by summing slip of
361 each SSE in each catalogue (Nishimura *et al.* 2013, Takagi *et al.* 2016, 2019). We then
362 evaluated the SSE slip rates by dividing the cumulative SSE slip at each grid by the analysis
363 period of each catalogue. The SSE slip rate indicates the activity of deep slow earthquakes.
364 We did not calculate SSE slip rates for shallow SSEs reported by Yokota & Ishikawa (2020)
365 because the number of detected events was still too low at each region. For similar reasons,
366 the long-term SSEs off the Kii Channel (Kobayashi 2014) and Tokai (Miyazaki *et al.* 2006)
367 regions were also excluded from the SSE slip rate calculation. Thus, we plotted the fault
368 configurations or large slip areas of long-term SSEs and shallow SSEs. We also plotted
369 shallow LFTs (Yamashita *et al.* 2015) and shallow VLFs (Takemura *et al.* 2019c) as
370 indicators of shallow slow earthquake activity. The spatial distribution of slip-deficit rates
371 from GNSS and GNSS-A observations by Noda *et al.* (2018), is plotted using blue contour
372 lines in Figure 11.

373 At deeper depths (30–40 km), deep slow earthquakes were active, especially in areas with
374 high SSE slip rates, but no interplate regular earthquakes were found. Although SSEs were
375 not removed in the slip-deficit rate estimation of Noda *et al.* (2018)—except for long-term
376 SSEs at the Bungo Channel—the regions with deep SSEs were characterised by low (20–40
377 mm/y) slip-deficit rates. At shallower depths (< 30 km) in the offshore region, regular
378 earthquakes, slow earthquakes, and high (> 60 mm/y) slip-deficit zones were separated from
379 each other. Similar separations of the repeating earthquakes, slow earthquakes, and large
380 coseismic slip areas of megathrust earthquakes at shallower depths were observed in the
381 regions of Tohoku (e.g., Nishikawa *et al.* 2019), Central Ecuador (e.g., Vaca *et al.* 2018) and
382 Costa Rica (e.g., Dixon *et al.* 2014). In particular, Nishikawa *et al.* (2019) pointed out that

383 slow earthquakes were complementarily distributed in the regions surrounding the large
384 coseismic slip area of the 2011 M_w 9.0 Tohoku earthquake. Takemura *et al.* (2019c) pointed
385 out that shallow, slow earthquakes cluster or migrate due to the existence of pore fluid in the
386 transitional regions between high-strength and low-strength zones of the plate boundary.
387 According to these previous studies and our observations, we suggest that the observed
388 separation between slip behaviours on the plate boundary along the Nankai Trough are
389 related to the heterogeneous distribution of effective strengths on the plate boundary, which is
390 controlled by the frictional coefficient, pore fluid pressure, and normal stress.

391

392 **4.2. Regional 3D CMT inversions for the M_w 7.2 and 7.5 earthquakes southeast off the** 393 **Kii Peninsula**

394 We conducted 3D CMT inversions of offshore earthquakes with M_w of 4.3–6.5. During
395 the analysis period (April 2004 to August 2019), M_w 7.2 and 7.5 intraslab earthquakes occurred
396 southeast off the Kii Peninsula on 5 September 2004. Because typical M_w 7 class earthquakes
397 have rupture durations of 30–50 s and fault areas of 1000–5000 km² (e.g. Kanamori & Brodsky
398 2004), precise source parameter estimation for such earthquakes is difficult based on our
399 assumptions of the CMT inversion. Despite these disadvantages, the rapid estimation of the
400 CMT solution for these large earthquakes is important for disaster mitigation, such as a CMT-
401 based tsunami warning system. We, therefore, tested our simple CMT inversion for the M_w 7.2
402 and 7.5 southeast off the Kii Peninsula earthquakes. Because amplitude saturation of F-net
403 broadband seismometers occurs for regional large earthquakes, we used F-net strong motion
404 seismometers, which have a large clip level and similar frequency response to STS-2
405 seismometers for periods less than 100 s. We selected F-net stations with distances of 200–500
406 km from the initial epicentre, which were slightly farther than for the original CMT settings
407 (100–400 km).

408 Figures 12 and 13 show the results of CMT inversions for the M_w 7.2 and 7.5 earthquakes
409 southeast off the Kii Peninsula, respectively. Detailed estimated parameters are also listed in
410 Table S2. Signal-to-noise ratios were high enough compared to smaller ($M_w < 4.5$)
411 earthquakes in this study but the VRs were low compared to those of moderate earthquakes.
412 The synthetic waveforms roughly corresponded to the observed ones (Figures 12b and 13b).
413 Due to the assumptions of a point source and simple-source time function, detailed
414 characteristics of the observed waveforms were not successfully reproduced. Furthermore,
415 the high (> 66%) VR areas were wider than the CMT results for moderate earthquakes within
416 the same region (Figure 3). The estimated deviatoric components were very similar to those
417 in the GCMT catalogue, but, especially in the result of the M_w 7.2 earthquake, a large

418 isotropic component appeared. Waveform fitting and large non-double couple components
419 suggest the likely complexity of the rupture processes and the source extents for the M_w 7.2
420 and 7.5 earthquakes. Estimated moment magnitudes were slightly smaller than those of the
421 GCMT catalogue as a result of the analysed period and the deeper centroid depths. Our
422 analysis periods were not significantly larger than the rupture durations of M_w 7 earthquakes,
423 leading to size underestimation. However, the regional 3D CMT method provides better
424 constraints of dips and depths for offshore earthquakes compared to 1D CMT systems
425 (Figures 3, 4, 5, 6, and 9), and our 3D grid search required only 15-20 minutes. These points
426 show the advantages for CMT-based tsunami prediction systems (e.g. Inazu *et al.* 2016,
427 Reymond *et al.* 2012). To obtain more accurate solutions, the CMT method with various
428 durations (e.g., Takemura *et al.* 2019b) or deconvolution method (e.g., Vallée *et al.* 2011)
429 should be implemented. Such sophisticated methods require more time to obtain solutions.

430 We compared our CMT result for the M_w 7.2 earthquake with the finite-fault model
431 (Okuwaki & Yagi 2018) conducted using teleseismic records based on Yagi & Fukahata
432 (2011). Our horizontal centroid location was very close to an area with large (> 3 m)
433 coseismic slips (Figure 14). The horizontal locations of the dominant slip and centroid
434 locations of the 3D CMT solution were shared. The centroid location also agreed with that
435 estimated by tsunami record (Satake *et al.* 2005). Thus, we think that the centroid location of
436 the M_w 7.2 earthquake was well constrained by our 3D CMT method. The depths of large
437 coseismic slips in the finite fault model ranged from 9 to 18 km, but the optimal centroid
438 depth of the 3D CMT inversion was 26 km. The depth difference could be due to the regional
439 3D heterogeneities (accretionary prism, bathymetry change, and subducting plate). According
440 to the hypocentre determinations derived using ocean-bottom seismometers (Nakano *et al.*
441 2015, Sakai *et al.* 2005), the hypocentres of aftershocks due to the M_w 7.5 earthquake were
442 distributed at depths of approximately 10–30 km. We also tested the centroid depth and large
443 isotropic components by our 3D CMT inversion. By using simulated seismograms of the
444 finite-fault model (Okuwaki & Yagi 2018) as observed seismograms, we conducted CMT
445 inversion of the simulated M_w 7.2 intraslab earthquake (Figure S6). The centroid location and
446 depth well corresponded to the large slip area of the finite-fault model. The large isotropic
447 component was also estimated. Thus, large non-double couple components suggest the likely
448 complexity of the rupture processes and the source extents for the finite-fault model of the
449 M_w 7.2 earthquake. Based on the hypocentre distribution of aftershocks, the fault dimensions
450 of the M_w 7.2 earthquake, and synthetic test, we considered that the extension of seismic slips

451 at depths of approximately 26 km might be possible.

452 The detailed rupture processes of the M_w 7.2 and 7.5 earthquakes remain unclear. The
453 regional seismic data and 3D Green's functions may provide additional constraints for large
454 offshore earthquakes. The finite fault modelling based on the 3D Green's functions is an
455 important but challenging issue that requires particular attention in future studies.

456

457 **5. Conclusion**

458 We conducted 3D CMT inversions of moderate earthquakes along the Nankai Trough
459 using the regional 3D Green's function dataset. By comparing 3D CMT solutions with those
460 in the F-net catalogue, large differences in focal mechanisms and centroid depths were found
461 for offshore earthquakes. These differences could be caused by 3D offshore heterogeneities,
462 such as the low-velocity accretionary prism and subducting Philippine Sea plate. Onshore
463 MT inversion using a simple 1D Earth model could provide incorrect estimations due to
464 offshore heterogeneities and station coverage. By introducing the effects of such 3D
465 heterogeneities, the 3D CMT solutions for offshore earthquakes practically agreed with
466 hypocentre distributions determined by ocean-bottom seismometers. Furthermore, our CMT
467 method based on onshore seismograms provided better constrained focal mechanisms and
468 centroid depths compared to the F-net MT catalogue. We also compared our CMT solutions
469 with those of the GCMT catalogue. The teleseismic CMT solutions are generally robust but
470 regional 3D CMT could provide better constraints of dip angles. The regional 3D CMT
471 catalogue contains more earthquakes compared to the GCMT catalogue, where only
472 earthquakes with about $M_w > 5$ are listed. To investigate detailed decade-scale seismicity in a
473 certain region, CMT inversion incorporating regional 3D velocity model should be required.

474 Although no suggestive interplate earthquakes are listed in the 1D catalogue, some low-
475 angle thrust faulting solutions at depths around the plate boundary were confirmed by our 3D
476 CMT catalogue. These earthquakes could be interpreted as interplate earthquakes. By using
477 our 3D CMT catalogue and previously published slow earthquake models, we illustrated the
478 spatial distribution of slip behaviours on the plate boundary along the Nankai Trough.
479 Regular interplate earthquakes and slow earthquakes occur within different segments on the
480 plate boundary. These separated distributions might reflect the heterogeneous distribution of
481 effective strength on the plate boundary. The gap zones, where no regular interplate and slow
482 earthquakes occurred, were found in the Nankai, Tonankai, and Tokai regions. These were the
483 regions with large (> 60 mm/y) slip-deficit rates, where the plate boundary can be strongly

484 coupled.

485 The regional CMT inversion of earthquakes with $M_w > 7$ was generally difficult due to
486 their fault size and the amplitude saturation of the broadband sensors. CMT inversions for the
487 2004 M_w 7.2 and 7.5 intraslab earthquakes southeast of the Kii Peninsula were performed
488 using the regional broadband strong motion sensors of F-net. Although signal-to-noise ratios
489 of the observed displacements were good enough, the waveform fittings of the M_w 7.2 and
490 7.5 intraslab earthquakes were not good compared to those of typical moderate earthquakes
491 due to fault sizes and the rupture complexity. However, the centroid location agreed with that
492 estimated by tsunami record, and the focal mechanism could be constrained. These points and
493 the rapid availability of a solution could be the advantages for CMT-based tsunami warning
494 systems.

495

496 **Acknowledgements**

497 F-net waveform data and the F-net MT catalogue are available via the website of the National
498 Research Institute for Earth Science and Disaster Resilience
499 (<https://doi.org/10.17598/NIED.0005>). Bathymetric depth data was obtained from ETOPO1
500 (Amante & Eakins 2009). OpenSWPC software (Maeda *et al.* 2017) and the 3D model of
501 Koketsu *et al.* (2012) were obtained from <https://github.com/takuto-maeda/OpenSWPC> and
502 https://www.jishin.go.jp/evaluation/seismic_hazard_map/lpshm/12_choshuki_dat/,
503 respectively. Generic Mapping Tools (Wessel *et al.* 2013) and Seismic Analysis Code (SAC;
504 Helffrich *et al.* 2013) were used to make the figures and when conducting the signal
505 processing work, respectively. The catalogue of slow earthquakes (Nishimura *et al.* 2013,
506 Takagi *et al.* 2016, Yamashita *et al.* 2015) was downloaded from the Slow Earthquake
507 Database website (Kano *et al.* 2018; <http://www-solid.eps.s.u-tokyo.ac.jp/~sloweql/>). Our
508 CMT catalogue and CMT results of assumed source grids for each earthquake are available
509 from <https://doi.org/10.5281/zenodo.3674161>. The FDM simulations of seismic wave
510 propagation were conducted on the computer system of the Earthquake and Volcano
511 Information Center at the Earthquake Research Institute, the University of Tokyo. This study
512 was supported by the Japan Society for the Promotion of Science (JSPS) KAKENHI Grant
513 Numbers 17K14382 under the Grant-in-Aid for Young Scientists (B) and 19H04626 in
514 Scientific Research under Innovative Areas ‘Science of Slow Earthquakes’. We also thank Dr
515 J. Braunmiller, an anonymous reviewer and Editor Prof. J. Virieux for careful reviewing and
516 constructive comments, which have helped to improve the manuscript.

517

518

519

520 **References**

- 521 Aki, K. & Richards, P. (2002) *Quantitative Seismology*, 2nd ed., University Science Books.
522 Retrieved from https://www.ldeo.columbia.edu/~richards/Aki_Richards.html
- 523 Amante, C. & Eakins, B.W. (2009) ETOPO1 1 arc-minute global relief model: Procedures,
524 data sources and analysis. NOAA Technical Memorandum NESDIS NGDC-24. *NOAA*
525 *Tech. Memo. NESDIS NGDC-24. Natl. Geophys. Data Center, NOAA*, 19.
526 doi:10.7289/V5C8276M
- 527 Ando, M. (1975) Source mechanisms and tectonic significance of historical earthquakes
528 along the Nankai trough, Japan. *Tectonophysics*, **27**, 119–140. doi:10.1016/0040-
529 1951(75)90102-X
- 530 Dixon, T.H., Jiang, Y., Malservisi, R., McCaffrey, R., Voss, N., Protti, M. & Gonzalez, V.
531 (2014) Earthquake and tsunami forecasts: Relation of slow slip events to subsequent
532 earthquake rupture. *Proc. Natl. Acad. Sci.*, **111**, 17039–17044.
533 doi:10.1073/pnas.1412299111
- 534 Dziewonski, A.M., Chou, T.-A. & Woodhouse, J.H. (1981) Determination of earthquake
535 source parameters from waveform data for studies of global and regional seismicity. *J.*
536 *Geophys. Res. Solid Earth*, **86**, 2825–2852. doi:10.1029/JB086iB04p02825
- 537 Eberhart-Phillips, D., Reyners, M., Bannister, S., Chadwick, M. & Ellis, S. (2010)
538 Establishing a versatile 3-D seismic velocity model for New Zealand. *Seismol. Res.*
539 *Lett.*, **81**, 992–1000. doi:10.1785/gssrl.81.6.992
- 540 Eisner, L. & Clayton, R.W. (2001) A reciprocity method for multiple-source simulations.
541 *Bull. Seismol. Soc. Am.*, **91**, 553–560. doi:10.1785/0120000222
- 542 Ekström, G., Nettles, M. & Dziewoński, A.M. (2012) The global CMT project 2004-2010:
543 Centroid-moment tensors for 13,017 earthquakes. *Phys. Earth Planet. Inter.*, **200–201**,
544 1–9. doi:10.1016/j.pepi.2012.04.002
- 545 Fukuyama, E., Ishida, M., Dreger, D.S. & Kawai, H. (1998) Automated seismic moment
546 tensor determination by using on-line broadband seismic waveforms. *Zisin*, **51**, 149–
547 156. doi:10.4294/zisin1948.51.1_149
- 548 Gokhberg, A. & Fichtner, A. (2016) Full-waveform inversion on heterogeneous HPC
549 systems. *Comput. Geosci.*, **89**, 260–268, Elsevier. doi:10.1016/j.cageo.2015.12.013
- 550 Gomberg, J. (2018) Cascadia Onshore-Offshore Site Response, Submarine Sediment
551 Mobilization, and Earthquake Recurrence. *J. Geophys. Res. Solid Earth*, **123**, 1381–
552 1404. doi:10.1002/2017JB014985
- 553 Hardebeck, J.L. & Shearer, P.M. (2002) A new method for determining first-motion focal
554 mechanisms. *Bull. Seismol. Soc. Am.*, **92**, 2264–2276. doi:10.1785/0120010200
- 555 Hejrani, B., Tkalčić, H. & Fichtner, A. (2017) Centroid moment tensor catalogue using a 3-D
556 continental scale Earth model: Application to earthquakes in Papua New Guinea and the
557 Solomon Islands. *J. Geophys. Res. Solid Earth*, **122**, 5517–5543.

558 doi:10.1002/2017JB014230

559 Helffrich, G., Wookey, J. & Bastow, I. (2013) *The Seismic Analysis Code*, Cambridge:
560 Cambridge University Press. doi:10.1017/CBO9781139547260

561 Helffrich, G.R. (1997) How good are routinely determined focal mechanisms? Empirical
562 statistics based on a comparison of Harvard, USGS and ERI moment tensors. *Geophys.*
563 *J. Int.*, **131**, 741–750. doi:10.1111/j.1365-246X.1997.tb06609.x

564 Hirose, F., Nakajima, J. & Hasegawa, A. (2008) Three-dimensional seismic velocity structure
565 and configuration of the Philippine Sea slab in southwestern Japan estimated by double-
566 difference tomography. *J. Geophys. Res. Solid Earth*, **113**, 1–26.
567 doi:10.1029/2007JB005274

568 Inazu, D., Pulido, N., Fukuyama, E., Saito, T., Senda, J. & Kumagai, H. (2016) Near-field
569 tsunami forecast system based on near real-time seismic moment tensor estimation in the
570 regions of Indonesia, the Philippines, and Chile 4. *Seismology. Earth, Planets Sp.*, **68**,
571 Springer Berlin Heidelberg. doi:10.1186/s40623-016-0445-x

572 Ito, Y. & Obara, K. (2006) Dynamic deformation of the accretionary prism excites very low
573 frequency earthquakes. *Geophys. Res. Lett.*, **33**, L02311. doi:10.1029/2005GL025270

574 Kamei, R., Pratt, R.G. & Tsuji, T. (2012) Waveform tomography imaging of a megasplay
575 fault system in the seismogenic Nankai subduction zone. *Earth Planet. Sci. Lett.*, **317–**
576 **318**, 343–353, Elsevier B.V. doi:10.1016/j.epsl.2011.10.042

577 Kanamori, H. & Brodsky, E.E. (2004) The physics of earthquakes. *Reports Prog. Phys.*, **67**,
578 1429–1496. doi:10.1088/0034-4885/67/8/R03

579 Kanamori, H. & Rivera, L. (2008) Source inversion of W phase: Speeding up seismic
580 tsunami warning. *Geophys. J. Int.*, **175**, 222–238. doi:10.1111/j.1365-
581 246X.2008.03887.x

582 Kaneko, Y., Ito, Y., Chow, B., Wallace, L.M., Tape, C., Grapenthin, R., D’Anastasio, E., *et*
583 *al.* (2019) Ultra-long Duration of Seismic Ground Motion Arising From a Thick, Low-
584 Velocity Sedimentary Wedge. *J. Geophys. Res. Solid Earth*, **124**, 10347–10359.
585 doi:10.1029/2019JB017795

586 Kano, M., Aso, N., Matsuzawa, T., Ide, S., Annoura, S., Arai, R., Baba, S., *et al.* (2018)
587 Development of a Slow Earthquake Database. *Seismol. Res. Lett.*, **89**, 1566–1575.
588 doi:10.1785/0220180021

589 Kikuchi, M. & Kanamori, H. (1991) Inversion of complex body waves-III. *Bull. Seism. Soc.*
590 *Am.*, **81**, 2335–2350. Retrieved from
591 [https://pubs.geoscienceworld.org/ssa/bssa/article/81/6/2335/102472/inversion-of-](https://pubs.geoscienceworld.org/ssa/bssa/article/81/6/2335/102472/inversion-of-complex-body-waves-iii)
592 [complex-body-waves-iii](https://pubs.geoscienceworld.org/ssa/bssa/article/81/6/2335/102472/inversion-of-complex-body-waves-iii)

593 Kimura, T., Murakami, H. & Matsumoto, T. (2015) Systematic monitoring of instrumentation
594 health in high-density broadband seismic networks. *Earth, Planets Sp.*, **67**, 55.
595 doi:10.1186/s40623-015-0226-y

596 Kobayashi, A. (2014) A long-term slow slip event from 1996 to 1997 in the Kii Channel,
597 *Japan. Earth, Planets Sp.*, **66**, 1–7. doi:10.1186/1880-5981-66-9

598 Koketsu, K., Miyake, H. & Suzuki, H. (2012) Japan Integrated Velocity Structure Model
599 Version 1. *Proc. 15th World Conf. Earthq. Eng.*, 1–4. Retrieved from
600 http://www.iitk.ac.in/nicee/wcee/article/WCEE2012_1773.pdf

601 Kubo, A., Fukuyama, E., Kawai, H. & Nonomura, K. (2002) NIED seismic moment tensor
602 catalogue for regional earthquakes around Japan: Quality test and application.
603 *Tectonophysics*, **356**, 23–48. doi:10.1016/S0040-1951(02)00375-X

604 Kubota, T., Suzuki, W., Nakamura, T., Chikasada, N.Y., Aoi, S., Takahashi, N. & Hino, R.
605 (2018) Tsunami source inversion using time-derivative waveform of offshore pressure
606 records to reduce effects of non-tsunami components. *Geophys. J. Int.*, **215**, 1200–1214,
607 Oxford University Press. doi:10.1093/GJI/GGY345

608 Kuge, K. & Kawakatsu, H. (1993) Significance of non-double couple components of deep
609 and intermediate-depth earthquakes: implications from moment tensor inversions of
610 long-period seismic waves. *Phys. Earth Planet. Inter.*, **75**, 243–266. doi:10.1016/0031-
611 9201(93)90004-S

612 Lee, S.-J., Liang, W.T., Cheng, H.W., Tu, F.S., Ma, K.F., Tsuruoka, H., Kawakatsu, H., *et al.*
613 (2013) Towards real-time regional earthquake simulation I: Real-time moment tensor
614 monitoring (RMT) for regional events in Taiwan. *Geophys. J. Int.*, **196**, 432–446.
615 doi:10.1093/gji/ggt371

616 Maeda, T., Takemura, S. & Furumura, T. (2017) OpenSWPC: an open-source integrated
617 parallel simulation code for modeling seismic wave propagation in 3D heterogeneous
618 viscoelastic media. *Earth, Planets Sp.*, **69**, 102, Springer Berlin Heidelberg.
619 doi:10.1186/s40623-017-0687-2

620 Miyazaki, S., Segall, P., McGuire, J.J., Kato, T. & Hatanaka, Y. (2006) Spatial and temporal
621 evolution of stress and slip rate during the 2000 Tokai slow earthquake. *J. Geophys. Res.*
622 *Solid Earth*, **111**, 1–17. doi:10.1029/2004JB003426

623 Nakanishi, A., Kodaira, S., Park, J.-O. & Kaneda, Y. (2002) Deformable backstop as seaward
624 end of coseismic slip in the Nankai Trough seismogenic zone. *Earth Planet. Sci. Lett.*,
625 **203**, 255–263. doi:10.1016/S0012-821X(02)00866-X

626 Nakano, M., Nakamura, T. & Kaneda, Y. (2015) Hypocenters in the nankai trough
627 determined by using data from both ocean-bottom and land seismic networks and a 3D
628 velocity structure model: Implications for seismotectonic activity. *Bull. Seismol. Soc.*
629 *Am.*, **105**, 1594–1605. doi:10.1785/0120140309

630 Nakano, M., Hyodo, M., Nakanishi, A., Yamashita, M., Hori, T., Kamiya, S., Suzuki, K., *et*
631 *al.* (2018a) The 2016 Mw 5.9 earthquake off the southeastern coast of Mie Prefecture as
632 an indicator of preparatory processes of the next Nankai Trough megathrust earthquake.
633 *Prog. Earth Planet. Sci.*, **5**, 30, Progress in Earth and Planetary Science.

634 doi:10.1186/s40645-018-0188-3

635 Nakano, M., Hori, T., Araki, E., Kodaira, S. & Ide, S. (2018b) Shallow very-low-frequency
636 earthquakes accompany slow slip events in the Nankai subduction zone. *Nat. Commun.*,
637 **9**, 984. doi:10.1038/s41467-018-03431-5

638 National Research Institute for Earth Science and Disaster Resilience. (2019) NIED F-net.
639 *Natl. Res. Inst. Earth Sci. Disaster Resil.* doi:10.17598/NIED.0005

640 Nishikawa, T., Matsuzawa, T., Ohta, K., Uchida, N., Nishimura, T. & Ide, S. (2019) The
641 slow earthquake spectrum in the Japan Trench illuminated by the S-net seafloor
642 observatories. *Science*, **365**, 808–813. doi:10.1126/science.aax5618

643 Nishimura, T., Matsuzawa, T. & Obara, K. (2013) Detection of short-term slow slip events
644 along the Nankai Trough, southwest Japan, using GNSS data. *J. Geophys. Res. Solid
645 Earth*, **118**, 3112–3125, Wiley-Blackwell. doi:10.1002/jgrb.50222

646 Noda, A., Saito, T. & Fukuyama, E. (2018) Slip-Deficit Rate Distribution Along the Nankai
647 Trough, Southwest Japan, With Elastic Lithosphere and Viscoelastic Asthenosphere. *J.
648 Geophys. Res. Solid Earth*, **123**, 8125–8142. doi:10.1029/2018JB015515

649 Okada, Y., Kasahara, K., Hori, S., Obara, K., Sekiguchi, S., Fujiwara, H. & Yamamoto, A.
650 (2004) Recent progress of seismic observation networks in Japan —Hi-net, F-net, K-
651 NET and KiK-net—. *Earth, Planets Sp.*, **56**, xv–xxviii. doi:10.1186/BF03353076

652 Okamoto, T., Takenaka, H. & Nakamura, T. (2018) Evaluation of accuracy of synthetic
653 waveforms for subduction-zone earthquakes by using a land–ocean unified 3D structure
654 model. *Earth, Planets Sp.*, **70**, Springer Berlin Heidelberg. doi:10.1186/s40623-018-
655 0871-z

656 Okuwaki, R. & Yagi, Y. (2018) Seismic source model for the Mw 7.2 2004 Kii peninsula,
657 Japan, earthquake. *Github*. doi:10.5281/zenodo.1493833

658 Park, J.-O., Fujie, G., Wijerathne, L., Hori, T., Kodaira, S., Fukao, Y., Moore, G.F., *et al.*
659 (2010) A low-velocity zone with weak reflectivity along the Nankai subduction zone.
660 *Geology*, **38**, 283–286. doi:10.1130/G30205.1

661 Ramos-Martínez, J. & McMechan, G.A. (2001) Source-parameter estimation by full
662 waveform inversion in 3D heterogeneous, viscoelastic, anisotropic media. *Bull. Seismol.
663 Soc. Am.*, **91**, 276–291. doi:10.1785/0120000017

664 Reymond, D., Okal, E.A., Hébert, H. & Bourdet, M. (2012) Rapid forecast of tsunami wave
665 heights from a database of pre-computed simulations, and application during the 2011
666 Tohoku tsunami in French Polynesia. *Geophys. Res. Lett.*, **39**, 1–6.
667 doi:10.1029/2012GL051640

668 Saito, T., Noda, A., Yoshida, K. & Tanaka, S. (2018) Shear strain energy change caused by
669 the interplate coupling along the Nankai Trough: An integration analysis using stress
670 tensor inversion and slip deficit inversion. *J. Geophys. Res. Solid Earth*.
671 doi:10.1029/2018JB015839

- 672 Sakai, S., Yamada, T., Shinohara, M., Hagiwara, H., Kanazawa, T., Obana, K., Kodaira, S.,
673 *et al.* (2005) Urgent aftershock observation of the 2004 off the Kii Peninsula earthquake
674 using ocean bottom seismometers. *Earth Planets Sp.*, **57**, 363–368.
675 doi:10.1186/BF03352577
- 676 Satake, K., Baba, T., Hirata, K., Iwasaki, S.I., Kato, T., Koshimura, S., Takenaka, J., *et al.*
677 (2005) Tsunami source of the 2004 off the Kii Peninsula earthquakes inferred from
678 offshore tsunami and coastal tide gauges. *Earth, Planets Sp.*, **57**, 173–178.
679 doi:10.1186/BF03351811
- 680 Shapiro, N.M., Campillo, M., Singh, S.K. & Pacheco, J. (1998) Seismic channel waves in the
681 accretionary prism of the Middle America Trench. *Geophys. Res. Lett.*, **25**, 101–104.
682 doi:10.1029/97GL03492
- 683 Shelly, D.R., Hardebeck, J.L., Ellsworth, W.L. & Hill, D.P. (2016) A new strategy for
684 earthquake focal mechanisms using waveform-correlation-derived relative polarities and
685 cluster analysis: Application to the 2014 Long Valley Caldera earthquake swarm. *J.*
686 *Geophys. Res. Solid Earth*, **121**, 8622–8641. doi:10.1002/2016JB013437
- 687 Shiomi, K., Obara, K. & Sato, H. (2006) Moho depth variation beneath southwestern Japan
688 revealed from the velocity structure based on receiver function inversion.
689 *Tectonophysics*, **420**, 205–221. doi:10.1016/j.tecto.2006.01.017
- 690 Storchak, D.A., Giacomo, D. Di, Bondár, I., Engdahl, E.R., Harris, J., Lee, W.H.K. &
691 Villaseñor, A. (2013) Public Release of the ISC – GEM Global Instrumental Earthquake
692 Catalogue (1900 – 2009). doi:10.1785/0220130034
- 693 Tahara, M., Uehira, K., Shimizu, H., Nakada, M., Yamada, T., Mochizuki, K., Shinohara, M.,
694 *et al.* (2008) Seismic velocity structure around the Hyuganada region, Southwest Japan,
695 derived from seismic tomography using land and OBS data and its implications for
696 interplate coupling and vertical crustal uplift. *Phys. Earth Planet. Inter.*, **167**, 19–33.
697 doi:10.1016/j.pepi.2008.02.001
- 698 Takagi, R., Obara, K. & Maeda, T. (2016) Slow slip event within a gap between tremor and
699 locked zones in the Nankai subduction zone. *Geophys. Res. Lett.*, **43**, 1066–1074.
700 doi:10.1002/2015GL066987
- 701 Takagi, R., Uchida, N. & Obara, K. (2019) Along-Strike Variation and Migration of Long-
702 Term Slow Slip Events in the Western Nankai Subduction Zone, Japan. *J. Geophys. Res.*
703 *Solid Earth*, **124**, 3853–3880. doi:10.1029/2018JB016738
- 704 Takemura, S., Shiomi, K., Kimura, T. & Saito, T. (2016) Systematic difference between first
705 - motion and waveform - inversion solutions for shallow offshore earthquakes due to a
706 low - angle dipping slab. *Earth, Planets Sp.*, 1–8, Springer Berlin Heidelberg.
707 doi:10.1186/s40623-016-0527-9
- 708 Takemura, S., Kimura, T., Saito, T., Kubo, H. & Shiomi, K. (2018a) Moment tensor
709 inversion of the 2016 southeast offshore Mie earthquake in the Tonankai region using a

710 three-dimensional velocity structure model: effects of the accretionary prism and
711 subducting oceanic plate. *Earth, Planets Sp.*, **70**, 50, Springer Berlin Heidelberg.
712 doi:10.1186/s40623-018-0819-3

713 Takemura, S., Matsuzawa, T., Kimura, T., Tonegawa, T. & Shiomi, K. (2018b) Centroid
714 Moment Tensor Inversion of Shallow Very Low Frequency Earthquakes Off the Kii
715 Peninsula, Japan, Using a Three-Dimensional Velocity Structure Model. *Geophys. Res.
716 Lett.*, **45**, 6450–6458. doi:10.1029/2018GL078455

717 Takemura, S., Kubo, H., Tonegawa, T., Saito, T. & Shiomi, K. (2019a) Modeling of Long-
718 Period Ground Motions in the Nankai Subduction Zone: Model Simulation Using the
719 Accretionary Prism Derived from Oceanfloor Local S-Wave Velocity Structures. *Pure
720 Appl. Geophys.*, **176**, 627–647, Birkhauser Verlag AG. doi:10.1007/s00024-018-2013-8

721 Takemura, S., Matsuzawa, T., Noda, A., Tonegawa, T., Asano, Y., Kimura, T. & Shiomi, K.
722 (2019b) Structural Characteristics of the Nankai Trough Shallow Plate Boundary
723 Inferred From Shallow Very Low Frequency Earthquakes. *Geophys. Res. Lett.*, **46**,
724 4192–4201, Blackwell Publishing Ltd. doi:10.1029/2019GL082448

725 Takemura, S., Noda, A., Kubota, T., Asano, Y., Matsuzawa, T. & Shiomi, K. (2019c)
726 Migrations and Clusters of Shallow Very Low Frequency Earthquakes in the Regions
727 Surrounding Shear Stress Accumulation Peaks Along the Nankai Trough. *Geophys. Res.
728 Lett.*, **46**, 11830–11840. doi:10.1029/2019GL084666

729 Terakawa, T. & Matsu'ura, M. (2010) The 3-D tectonic stress fields in and around Japan
730 inverted from centroid moment tensor data of seismic events. *Tectonics*, **29**, 1–14.
731 doi:10.1029/2009TC002626

732 Townend, J. & Zoback, M.D. (2006) Stress, strain, and mountain building in central Japan. *J.
733 Geophys. Res. Solid Earth*, **111**, 1–11. doi:10.1029/2005JB003759

734 Vaca, S., Vallée, M., Nocquet, J.M., Battaglia, J. & Régnier, M. (2018) Recurrent slow slip
735 events as a barrier to the northward rupture propagation of the 2016 Pedernales
736 earthquake (Central Ecuador). *Tectonophysics*, **724–725**, 80–92, Elsevier.
737 doi:10.1016/j.tecto.2017.12.012

738 Vallée, M., Charléty, J., Ferreira, A.M.G., Delouis, B. & Vergoz, J. (2011) SCARDEC: A
739 new technique for the rapid determination of seismic moment magnitude, focal
740 mechanism and source time functions for large earthquakes using body-wave
741 deconvolution. *Geophys. J. Int.*, **184**, 338–358. doi:10.1111/j.1365-246X.2010.04836.x

742 Wallace, L.M., Araki, E., Saffer, D., Wang, X., Roesner, A., Kopf, A., Nakanishi, A., *et al.*
743 (2016) Near-field observations of an offshore M w 6.0 earthquake from an integrated
744 seafloor and subseafloor monitoring network at the Nankai Trough, southwest Japan. *J.
745 Geophys. Res. Solid Earth*, **121**, 8338–8351. doi:10.1002/2016JB013417

746 Wang, X. & Zhan, Z. (2020) Moving from 1-D to 3-D velocity model: automated waveform-
747 based earthquake moment tensor inversion in the Los Angeles region. *Geophys. J. Int.*,

748 **220**, 218–234. doi:10.1093/gji/ggz435

749 Wessel, P., Smith, W.H.F., Scharroo, R., Luis, J. & Wobbe, F. (2013) Generic mapping tools:
750 Improved version released. *Eos (Washington. DC)*., **94**, 409–410.
751 doi:10.1002/2013EO450001

752 Yagi, Y., Kikuchi, M., Yoshida, S. & Yamanaka, Y. (1998) Source Process of the Hyuga-
753 nada Earthquake of April 1, 1968 (MJMA 7.5), and its Relationship to the Subsequent
754 Seismicity. *Zisin (Journal Seismol. Soc. Japan. 2nd ser.)*, **51**, 139–148.
755 doi:10.4294/zisin1948.51.1_139

756 Yagi, Y. & Fukahata, Y. (2011) Introduction of uncertainty of Green’s function into
757 waveform inversion for seismic source processes. *Geophys. J. Int.*, **186**, 711–720.
758 doi:10.1111/j.1365-246X.2011.05043.x

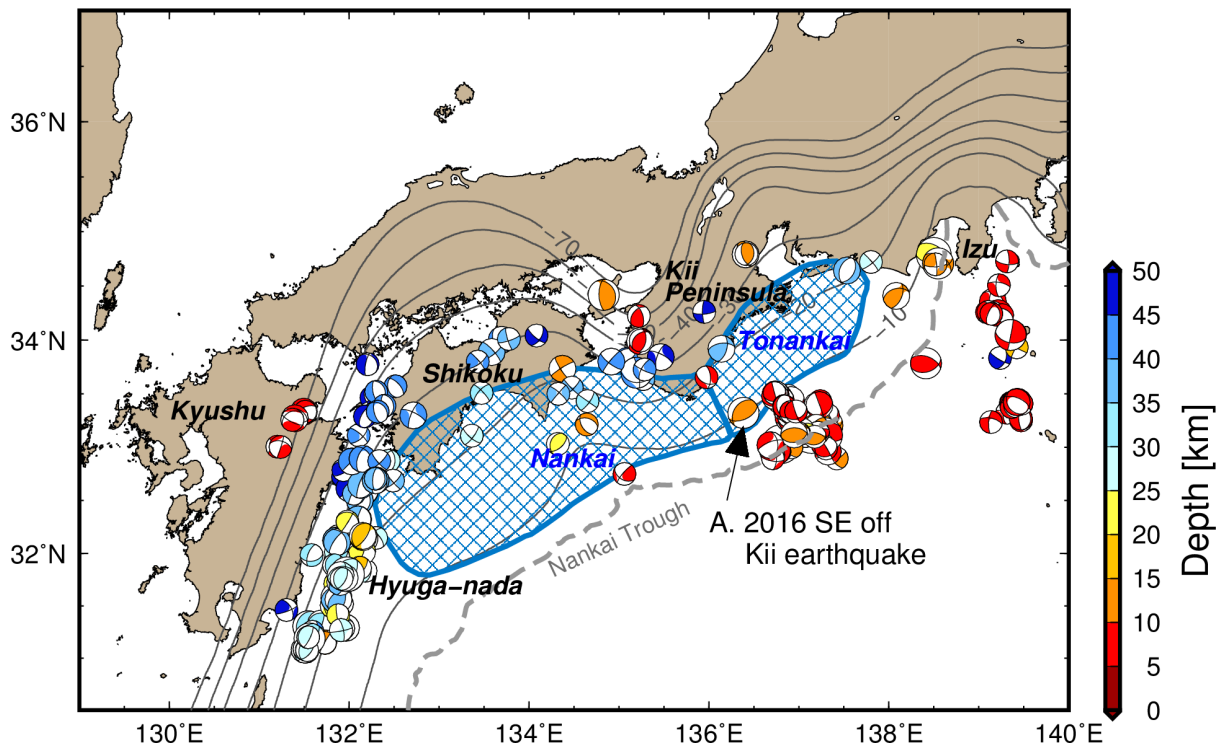
759 Yamashita, Y., Shimizu, H. & Goto, K. (2012) Small repeating earthquake activity, interplate
760 quasi-static slip, and interplate coupling in the Hyuga-nada, southwestern Japan
761 subduction zone. *Geophys. Res. Lett.*, **39**, 1–5. doi:10.1029/2012GL051476

762 Yamashita, Y., Yakiwara, H., Asano, Y., Shimizu, H., Uchida, K., Hirano, S., Umakoshi, K.,
763 *et al.* (2015) Migrating tremor off southern Kyushu as evidence for slow slip of a
764 shallow subduction interface. *Science*, **348**, 676–679. doi:10.1126/science.aaa4242

765 Yokota, Y. & Ishikawa, T. (2020) Shallow slow slip events along the Nankai Trough detected
766 by GNSS-A. *Sci. Adv.*, **6**, eaay5786. doi:10.1126/sciadv.aay5786

767

768

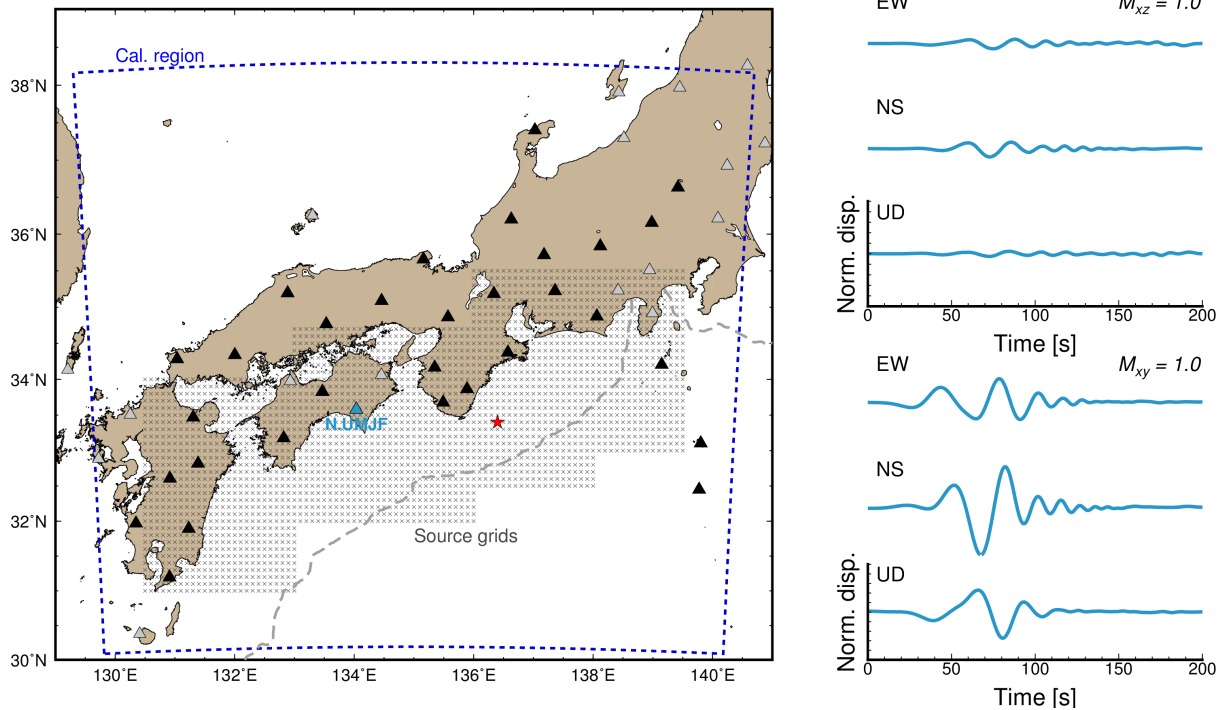


770

771 Figure 1. Map of the study region. The black contour lines are the iso-depth contour lines of
 772 the upper surface of the Philippine Sea Plate of Koketsu *et al.* (2012). Focal mechanisms
 773 are the moment tensor (MT) solutions of regular earthquakes with M_w of 4.3–6.5 in the
 774 F-net catalogue (Fukuyama *et al.* 1998, Kubo *et al.* 2002) that occurred in the area with
 775 latitudes less than 34.8°N , longitudes greater than 131°E , and at depths of less than 50
 776 km. The plotted MT solutions range from April 2004 to August 2019. The blue hatched
 777 areas represent the expected source region of the Nankai and Tonankai earthquakes
 778 (Earthquake Research Committee, 2001, available at:
 779 http://www.jishin.go.jp/main/chousa/01sep_nankai/index.htm). The earthquake marked A
 780 is the M_w 5.8 southeast off Kii Peninsula earthquake that occurred on 1 April 2016.

781

782



783

784 Figure 2. Calculation settings used in this study were the blue dashed line represents the

785 horizontal coverage of the simulation model region. The triangles and crosses in the map

786 denote the locations of the F-net stations and the assumed source grids, respectively.

787 Green's functions from the source grids to the black-fill and blue-fill triangles were

788 evaluated via reciprocal calculations using OpenSWPC code (Maeda *et al.* 2017). The

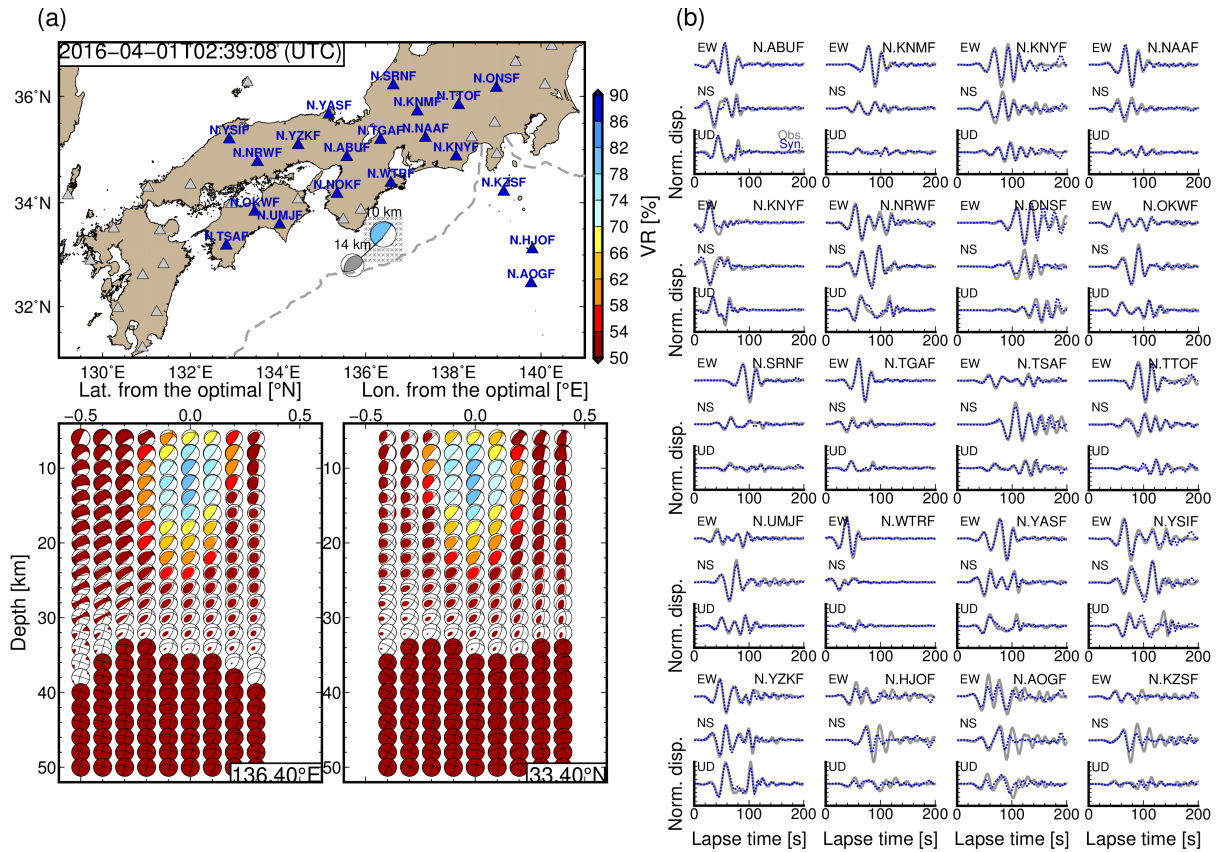
789 right-hand panels show examples of filtered displacement Green's functions from a

790 certain hypocentre (red star, at a depth of 10 km) to the N.UMJF station (blue triangle),

791 whose epicentral distance is 263 km. The filter passband was 25—100 s.

792

793



794

795

796

797

798

799

800

801

802

803

804

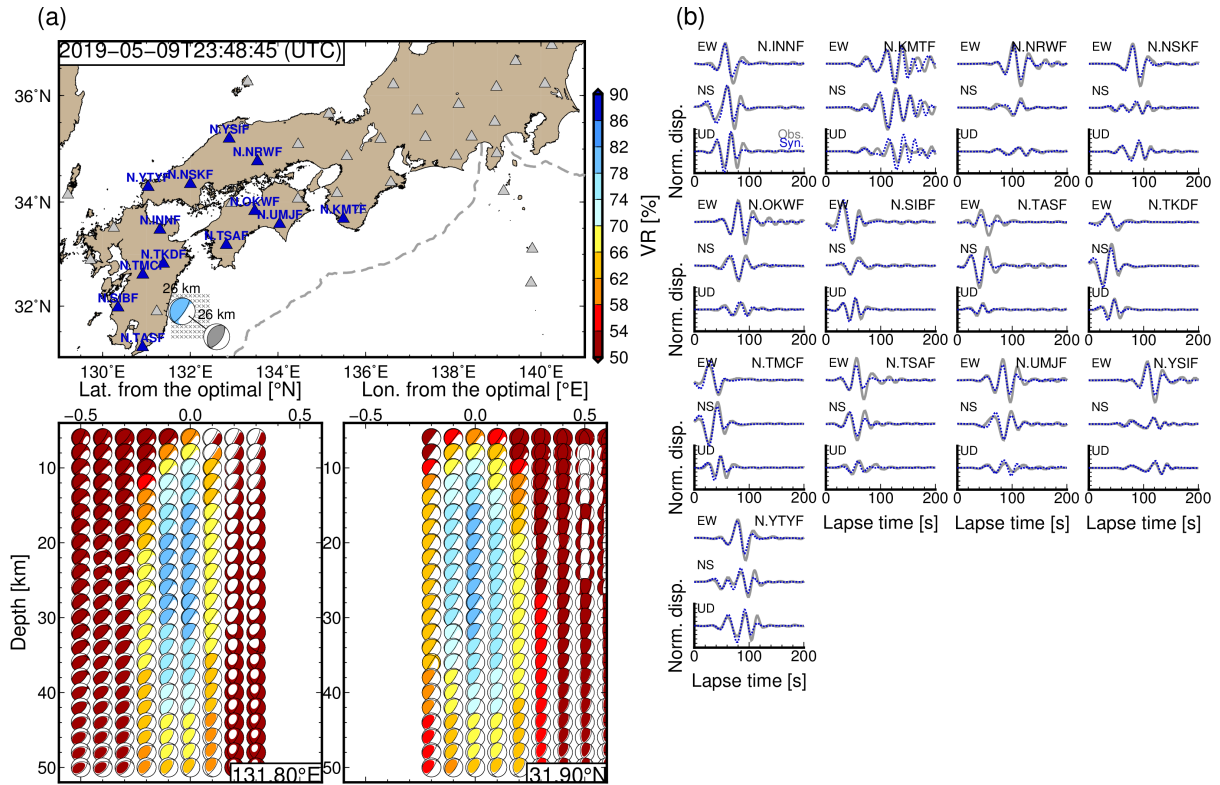
805

806

807

808

Figure 3. CMT results for the southeast off Kii Peninsula earthquake that occurred on 1 April 2016. (a) Locations of the optimal solutions, used stations, and depth variations of optimal solutions at each source grid. Colours of the focal mechanisms reflect values of variance reduction between observed and synthetic displacements in the 25–100 s period band. The numbers above the optimal solutions in (a) are the optimal centroid depths. The grey focal mechanism in (a) is the F-net MT solution of this earthquake. (b) Comparisons of observed and synthetic displacements in the 25–100 s period band. Grey solid and blue dotted lines are the observed and synthetic seismograms, respectively. Synthetic seismograms were evaluated by assuming the optimal solution. Amplitudes at each station were normalised by the maximum amplitude of both observed and synthetic three-component displacement waveforms. Detailed source parameters are listed in Table S1.



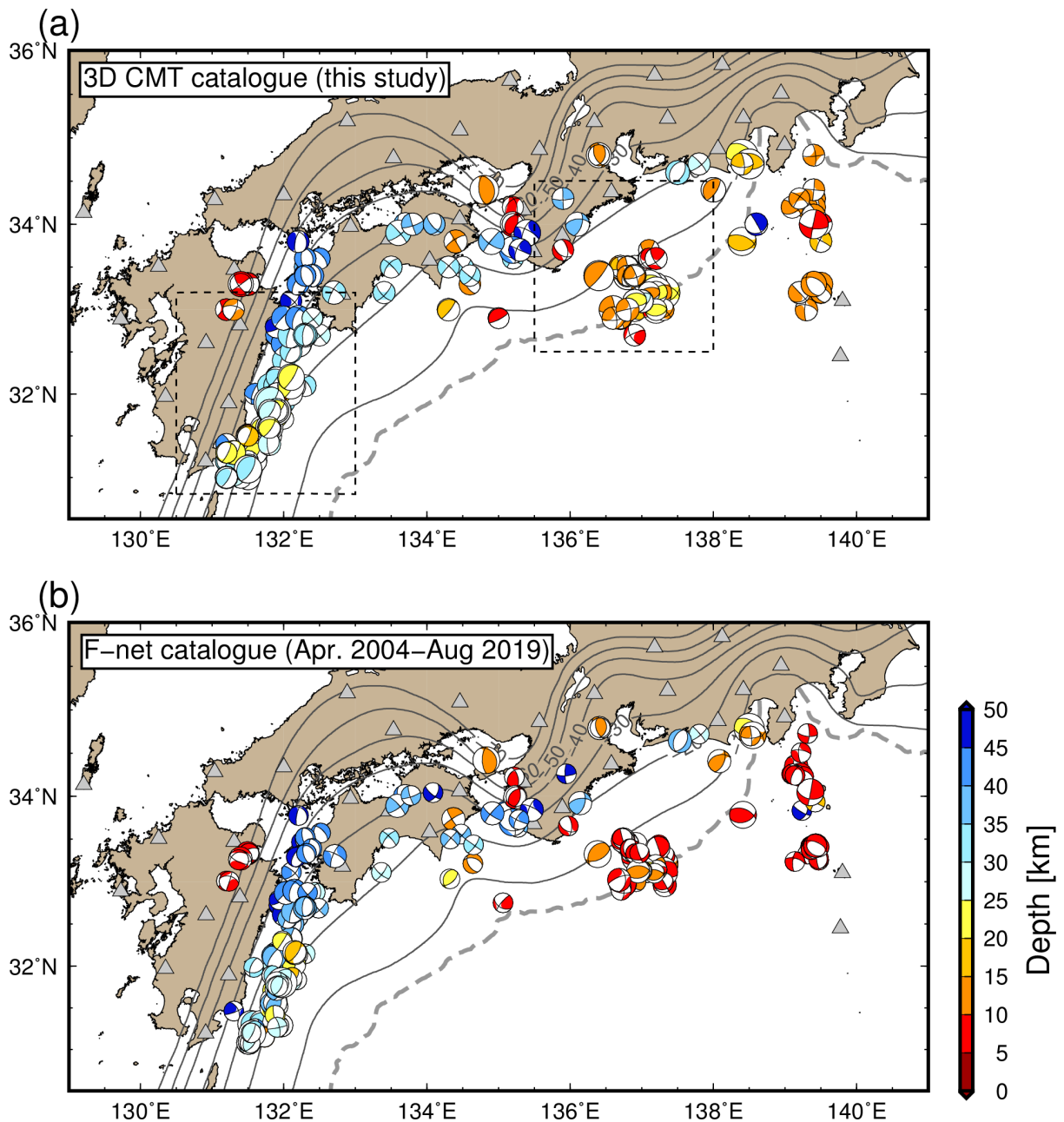
809

810 Figure 4. CMT results for the Hyuga-nada earthquake that occurred on 9 May 2019. (a)
 811 Locations of the optimal solutions, used stations, and depth variations of optimal
 812 solutions at each source grid. Colours of the focal mechanisms reflect values of variance
 813 reduction between observed and synthetic displacements in the 25–100 s period band.
 814 The numbers above the optimal solutions in (a) are the optimal centroid depths. The grey
 815 focal mechanism in (a) is the F-net MT solution of this earthquake. (b) Comparisons of
 816 observed and synthetic displacements in the 25–100 s period band. Grey solid and blue
 817 dotted lines are the observed and synthetic seismograms, respectively. Synthetic
 818 seismograms were evaluated by assuming the optimal solution. Amplitudes at each
 819 station were normalised by the maximum amplitude of both observed and synthetic
 820 three-component displacement waveforms. Detailed source parameters are listed in Table
 821 S1.

822

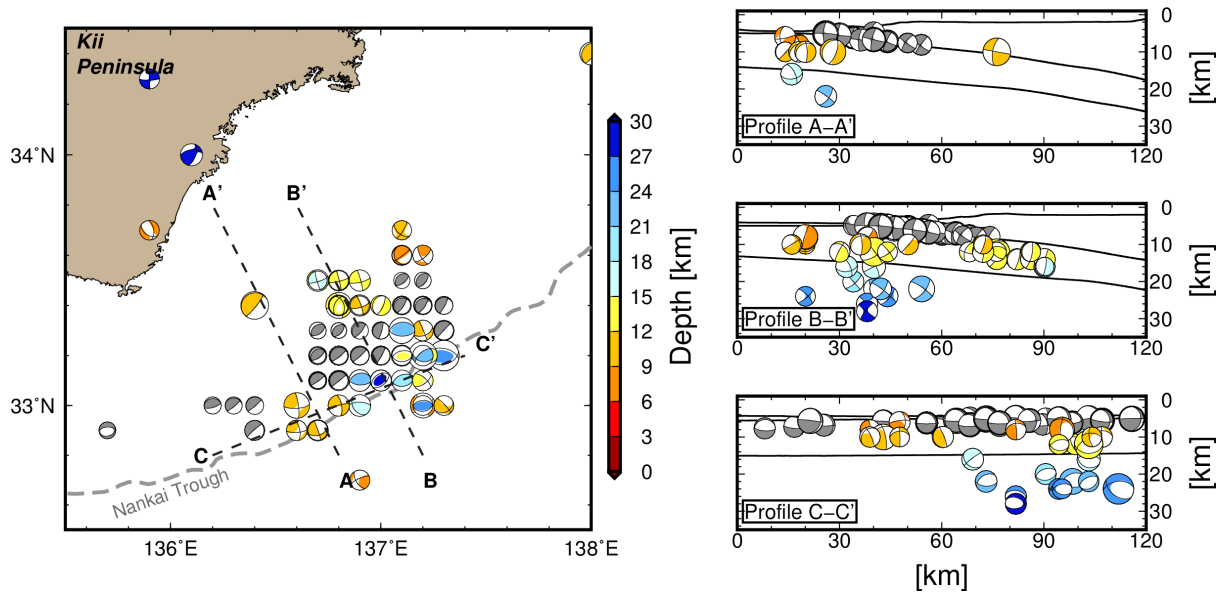
823

824



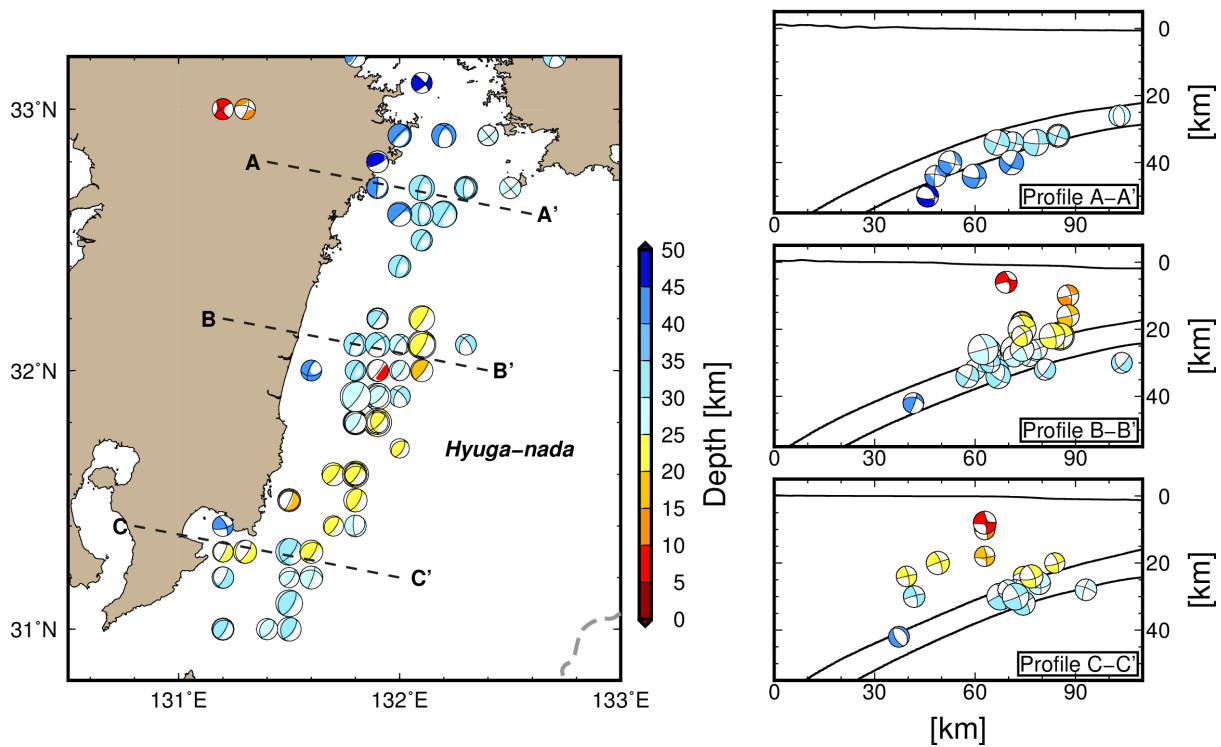
825
 826 Figure 5. Comparisons of estimated CMT solutions between the (a) 3D CMT and (b) F-net
 827 MT catalogues. Colours of focal mechanisms represent the centroid depths of each
 828 solution. Detailed source parameters of our 3D CMT solutions are listed in Table S1. The
 829 regions enclosed by the dashed lines in (a) are enlarged in Figures 6 and 7.

830
 831
 832



833

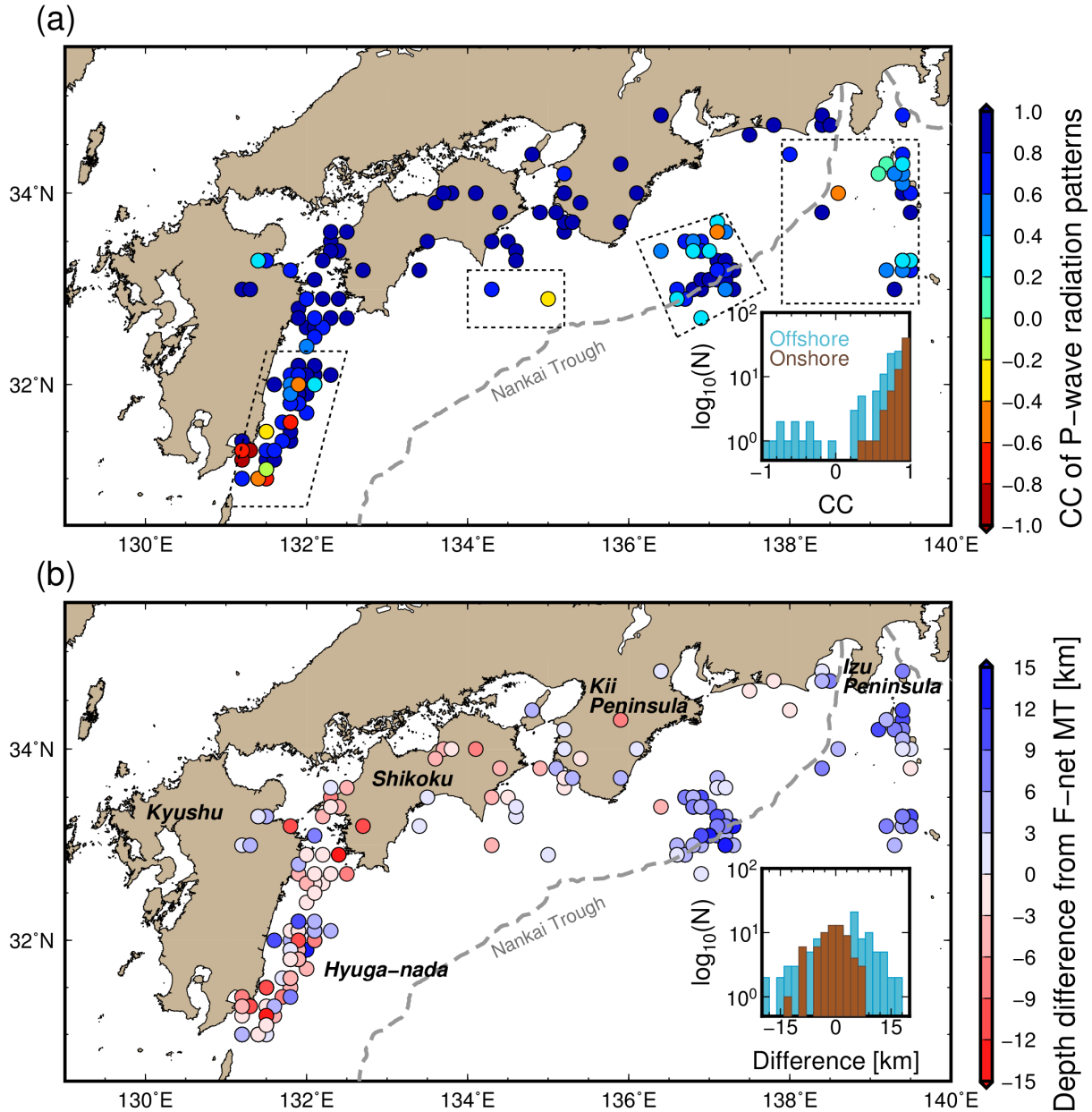
834 Figure 6. Spatial distribution of the CMT solutions southeast of the Kii Peninsula. Coloured
 835 focal mechanisms are our CMT solutions. Grey focal mechanisms are the CMT solutions
 836 of shallow VLFs (Takemura *et al.* 2019b). The right-hand panels show cross-sections
 837 along profiles A-A', B-B' and C-C'. The bathymetry of ETOPO1 (Amante & Eakins
 838 2009), the upper surface, and oceanic Moho of the Philippine Sea Plate (Koketsu *et al.*
 839 2012) along each profile are plotted in the right-hand panels.



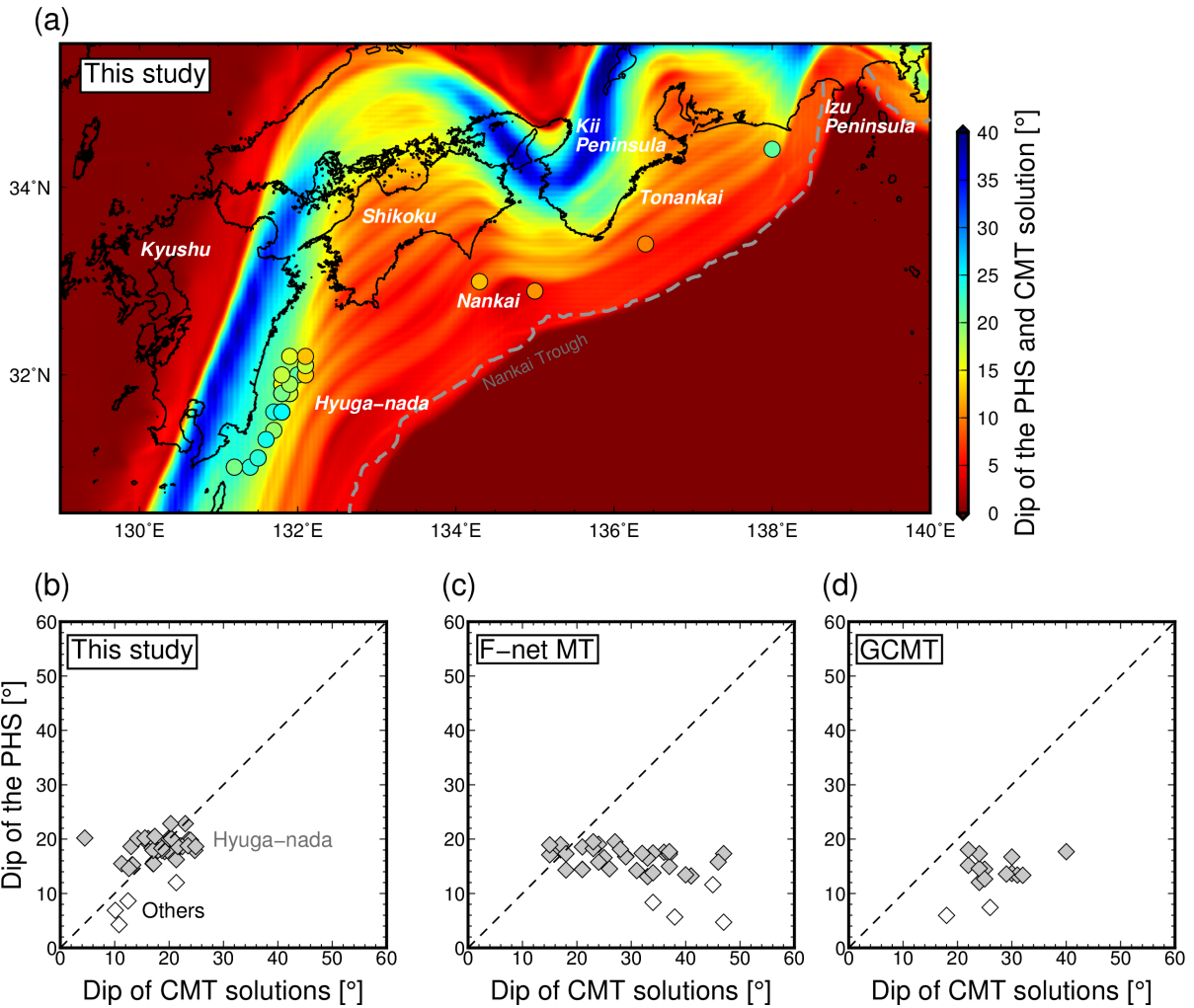
840

841 Figure 7. CMT results for the Hyuga-nada region. Coloured focal mechanisms are our CMT
 842 solutions. The right-hand panels show cross-sections along profiles A-A', B-B' and C-C'.

843 The bathymetry of ETOPO1 (Amante & Eakins 2009), the upper surface, and oceanic
 844 Moho of the Philippine Sea Plate (Koketsu *et al.* 2012) along each profile are plotted in
 845 the right-hand panels.
 846



847
 848 Figure 8. Spatial distributions of (a) correlation coefficients (CCs) of *P*-wave radiation
 849 patterns between 3D CMT and F-net solutions and (b) depth differences of 3D CMT
 850 solutions from the F-net catalogue. Lower right panels in (a) and (b) show histograms of
 851 CCs and differences, respectively. Offshore earthquakes are defined as earthquakes that
 852 occurred within regions closed by dotted lines in (a).
 853



854

855

856

857

858

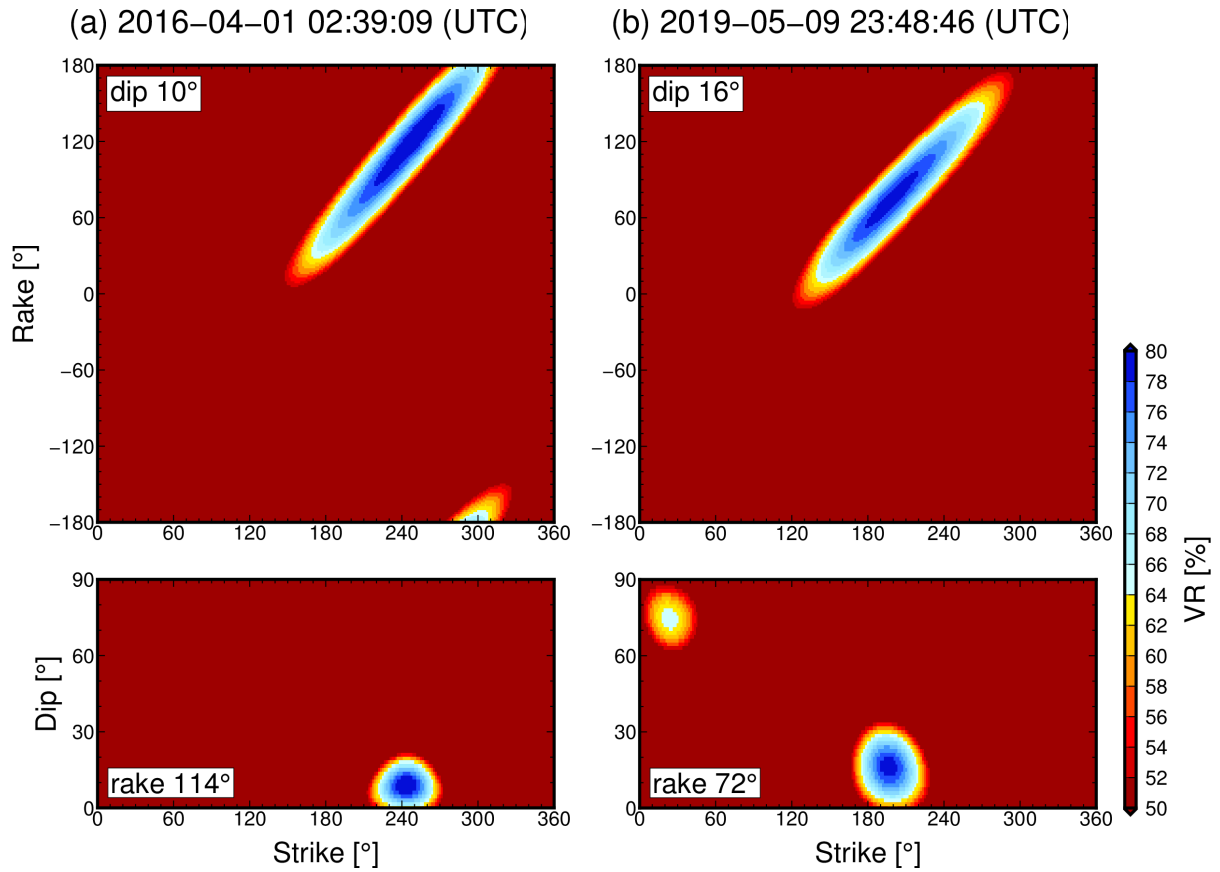
859

860

861

862

Figure 9. Comparisons of dip angles between the Philippine Sea plate (PHS) and CMT solutions for suggestive interplate earthquakes. (a) Map of the region, comparisons of dip angles of the Philippine Sea plate with (b) CMT solutions of this study and (c) F-net MT solutions. The background colour in (a) represents the spatial distribution of dip angles of the Philippine Sea plate. The coloured circles denote dip angles of CMT solutions in this study. We compared dip angles between the Philippine Sea plate and (c) F-net MT and (d) GCMT solutions of corresponding earthquakes.



863

864

865

866

867

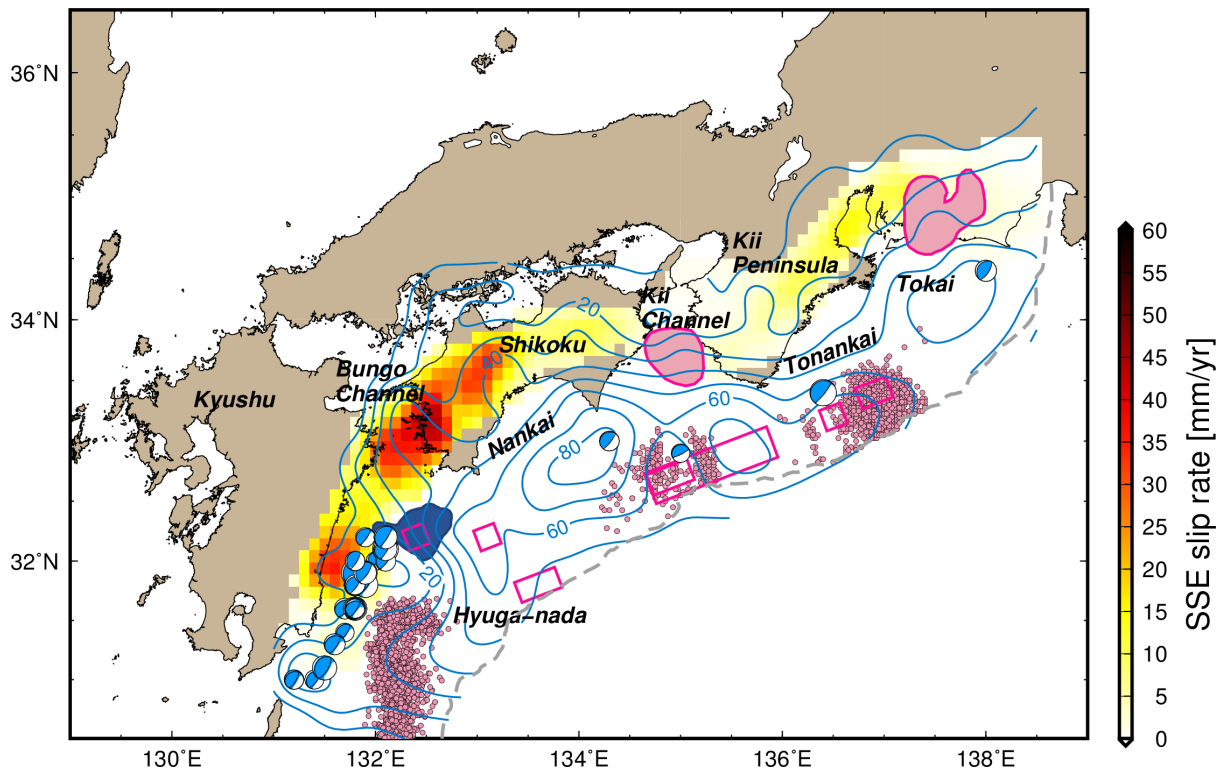
868

869

870

871

Figure 10. Distributions of variance reductions (VR) in the strike-rake and strike-dip planes for (a) the southeast off Kii Peninsula earthquake on 1 April 2016 and (b) the Hyuganada earthquake on 9 May 2019. In synthetics of displacement seismograms with various strike, dip, and rake, we assumed pure double-couple point sources and fixed hypocenter locations and seismic moments from CMT results (Figures 3 and 4).



872

873

874

875

876

877

878

879

880

881

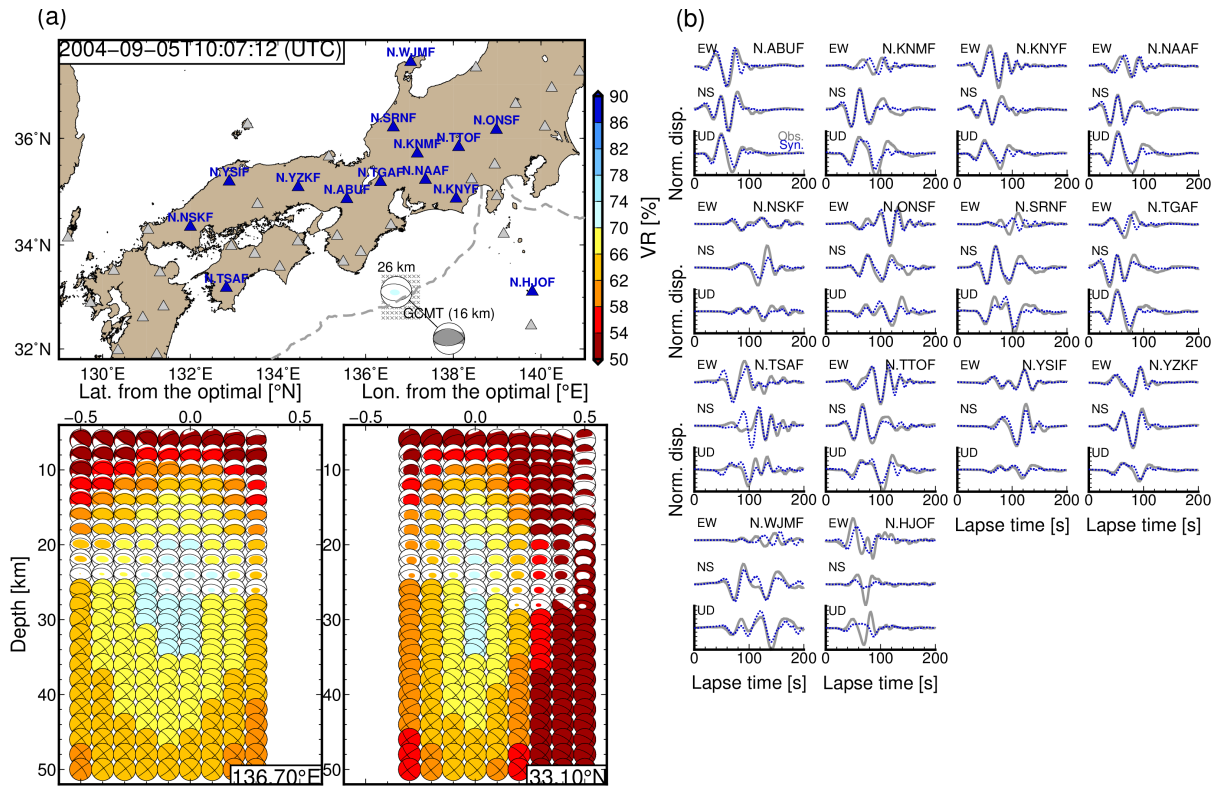
882

883

884

885

Figure 11. Spatial distribution of slip behaviours on the plate boundary along the Nankai Trough. Plotted focal mechanisms are low-angle thrust faulting solutions at depths around the plate boundary. The coseismic slip area of the 1968 M_w 7.5 Hyuga-nada earthquake (Yagi *et al.* 1998) is shaded in dark blue. SSE slip rates were evaluated from the combined SSE catalogues (Nishimura *et al.* 2013, Takagi *et al.* 2016, 2019). The pink circles indicate the epicentres of the shallow LFTs of the Hyuga-nada and the shallow VLFs in the Tonankai region referred from Yamashita *et al.* (2015) and Takemura, Noda, *et al.* (2019). The pink shaded areas and pink rectangles indicate the large slip areas of long-term SSEs (Kobayashi 2014, Miyazaki *et al.* 2006) and shallow SSEs (Yokota & Ishikawa 2020), respectively. The blue contour lines indicate the slip-deficit rates [mm/yr] on the plate boundary by Noda *et al.* (2018)



886

887

Figure 12. CMT results for the M_w 7.2 southeast off the Kii Peninsula earthquake that

888

occurred on 5 September 2004. Grey focal mechanisms are the solutions of the F-net MT

889

and GCMT catalogues. (a) Locations of the optimal solutions, used stations, and depth

890

variations of optimal solutions at each source grid. Colours of the focal mechanisms

891

reflect values of variance reduction between observed and synthetic displacements in the

892

25–100 s period band. The numbers above the optimal solutions in (a) are the optimal

893

centroid depths. The grey focal mechanism in (a) is the F-net MT solution of this

894

earthquake; (b) Comparisons of observed and synthetic displacements in the 25–100 s

895

period bands. Grey solid and blue dotted lines are the observed and synthetic

896

seismograms, respectively. Synthetic seismograms were evaluated by assuming the

897

optimal solution. Amplitudes at each station were normalised by the maximum amplitude

898

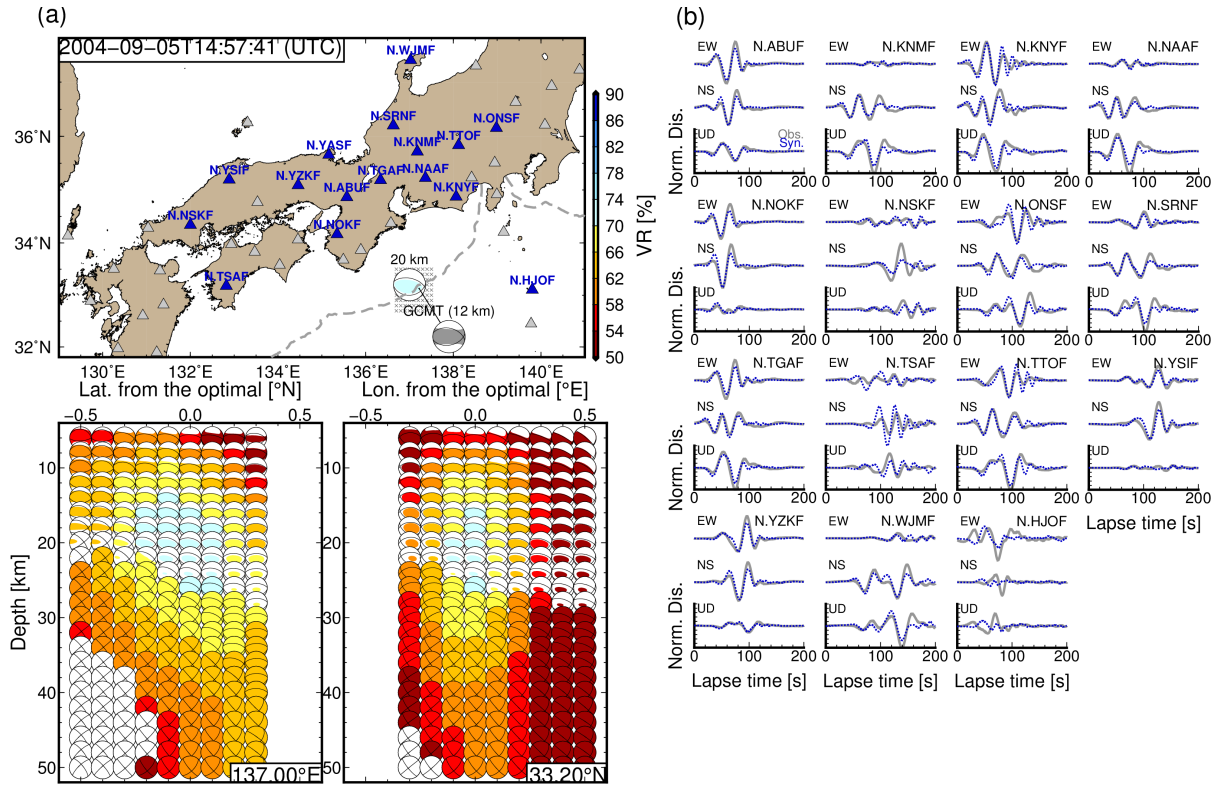
of both observed and synthetic three-component displacement waveforms. Detailed

899

source parameters are listed in Table S2.

900

901



902

903

Figure 13. CMT results for the M_w 7.5 southeast off the Kii Peninsula earthquake that

904

occurred on 5 September 2004. (a) Locations of the optimal solutions, used stations, and

905

depth variations of optimal solutions at each source grid. Colours of the focal

906

mechanisms reflect values of variance reduction between observed and synthetic

907

displacements in the 25–100 s period bands. The numbers above the optimal solutions in

908

(a) are the optimal centroid depths. The grey focal mechanism in (a) is the F-net MT

909

solution of this earthquake; (b) Comparisons of observed and synthetic displacements in

910

the 25–100 s period band. Grey solid and blue dotted lines are the observed and synthetic

911

seismograms, respectively. Synthetic seismograms were evaluated by assuming the

912

optimal solution. Amplitudes at each station were normalised by the maximum amplitude

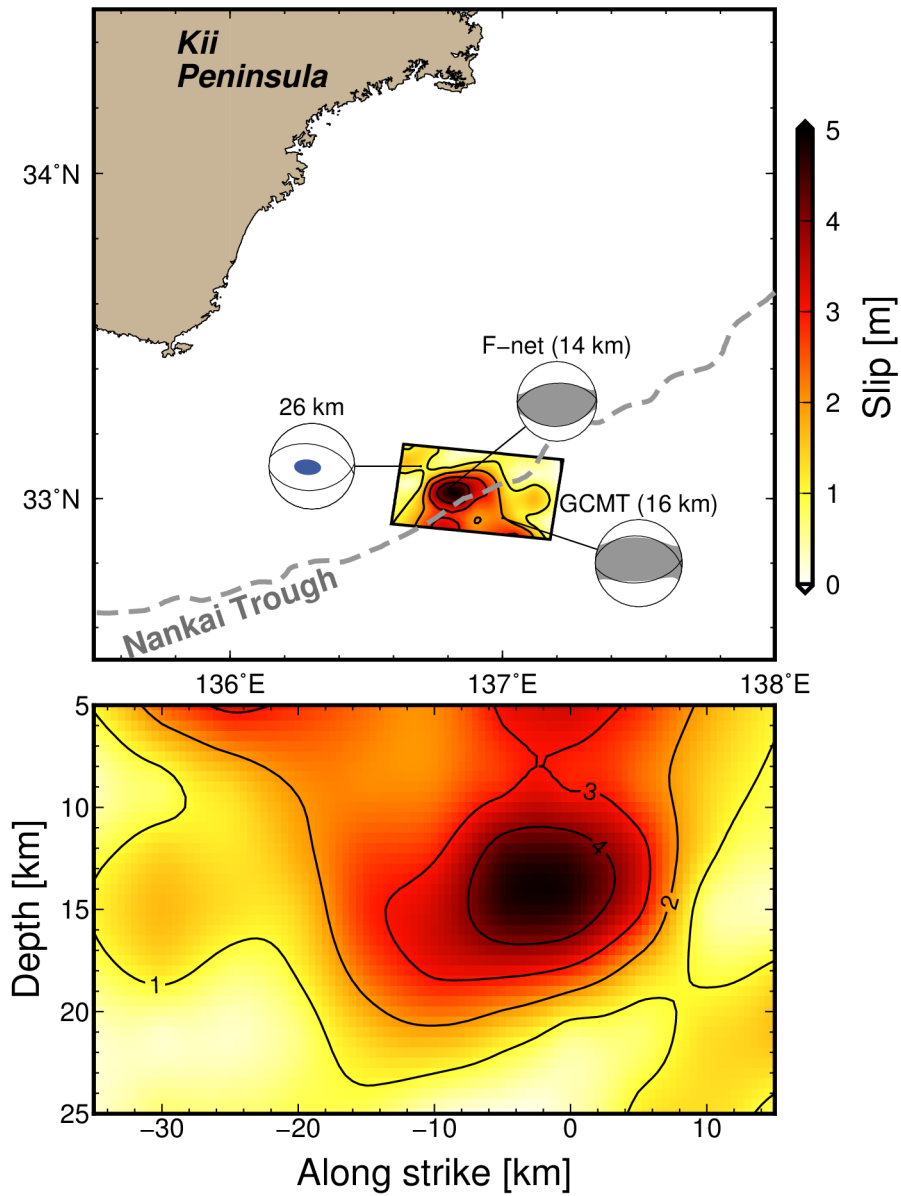
913

of both observed and synthetic three-component displacement waveforms. Detailed

914

source parameters are listed in Table S2.

915



916

917 Figure 14. Comparison of the CMT results for the M_w 7.2 southeast off the Kii Peninsula
 918 earthquake and other CMT catalogues (Ekström *et al.* 2012, Fukuyama *et al.* 1998, Kubo
 919 *et al.* 2002) and finite fault modelling (Okuwaki & Yagi 2018) solutions. The bottom
 920 panel is the slip distribution of the finite fault model in the strike-depth plane.

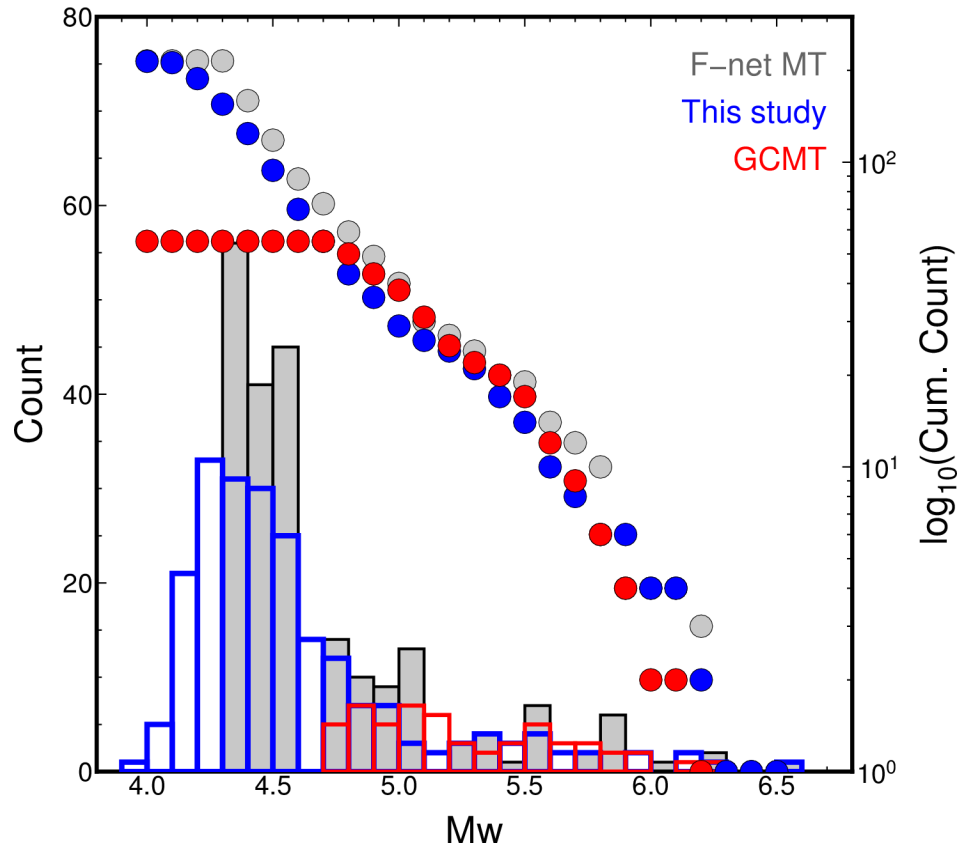


Figure S1. Size distribution of our 3D CMT catalogue (blue), the F-net catalogue (grey), and the GCMT catalogue (red). The selected criteria of the F-net and GCMT catalogue is same as in Figure 1.

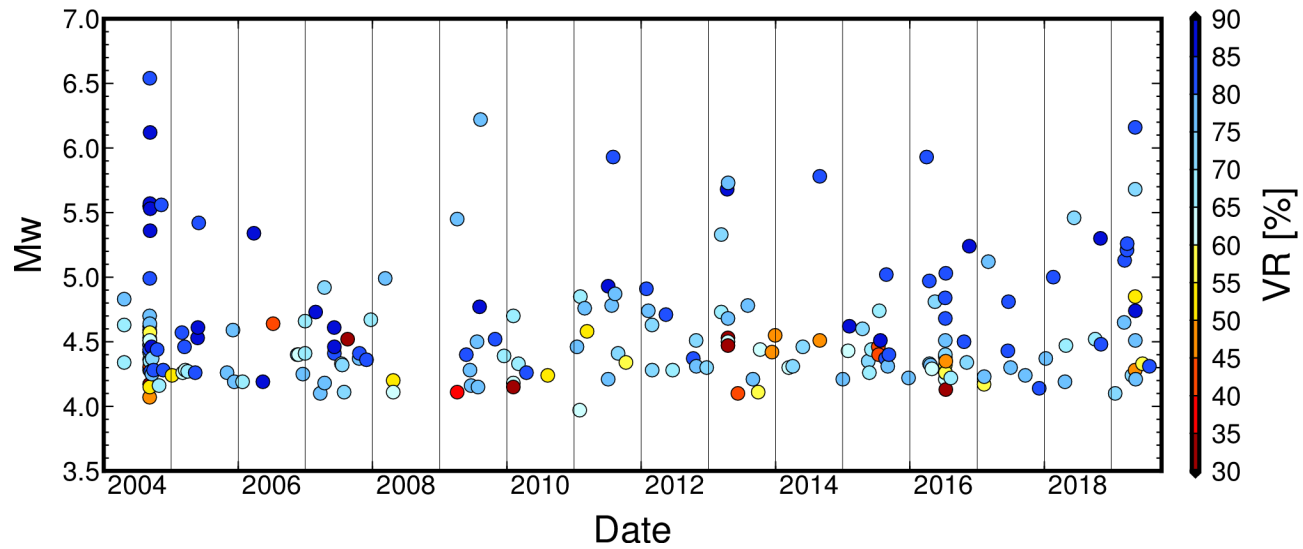


Figure S2. Magnitude-time diagram of our 3D CMT catalogue.

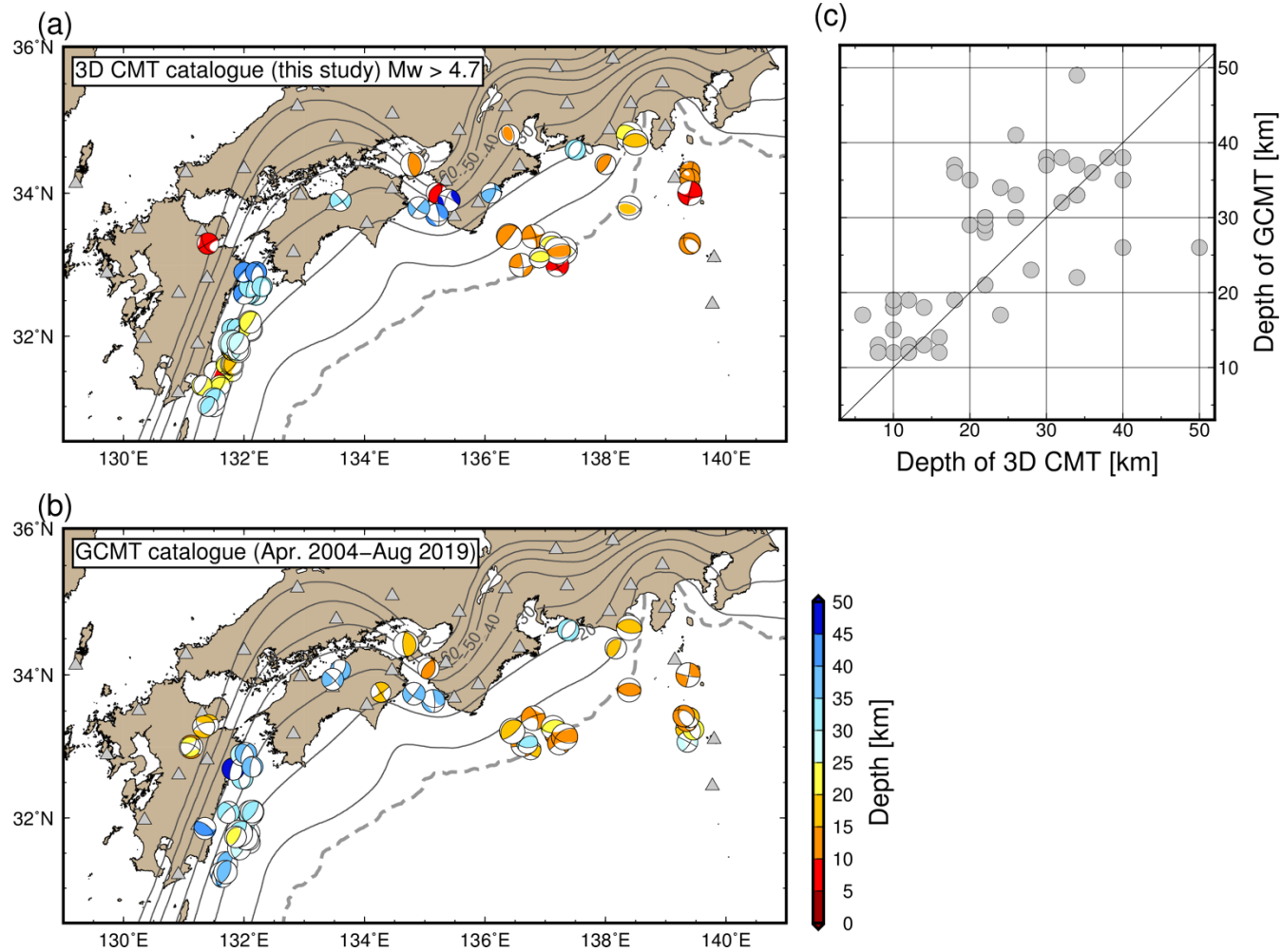


Figure S3. Similar as Figure 5 but for comparison with the GCMT catalogue. The M_w of plotted earthquakes in our 3D CMT catalogue is larger than 4.7, which is the lower limit of the GCMT catalogue (see Figure S1). We compared centroid depths of our CMT solutions with corresponding GCMT solutions in (c).

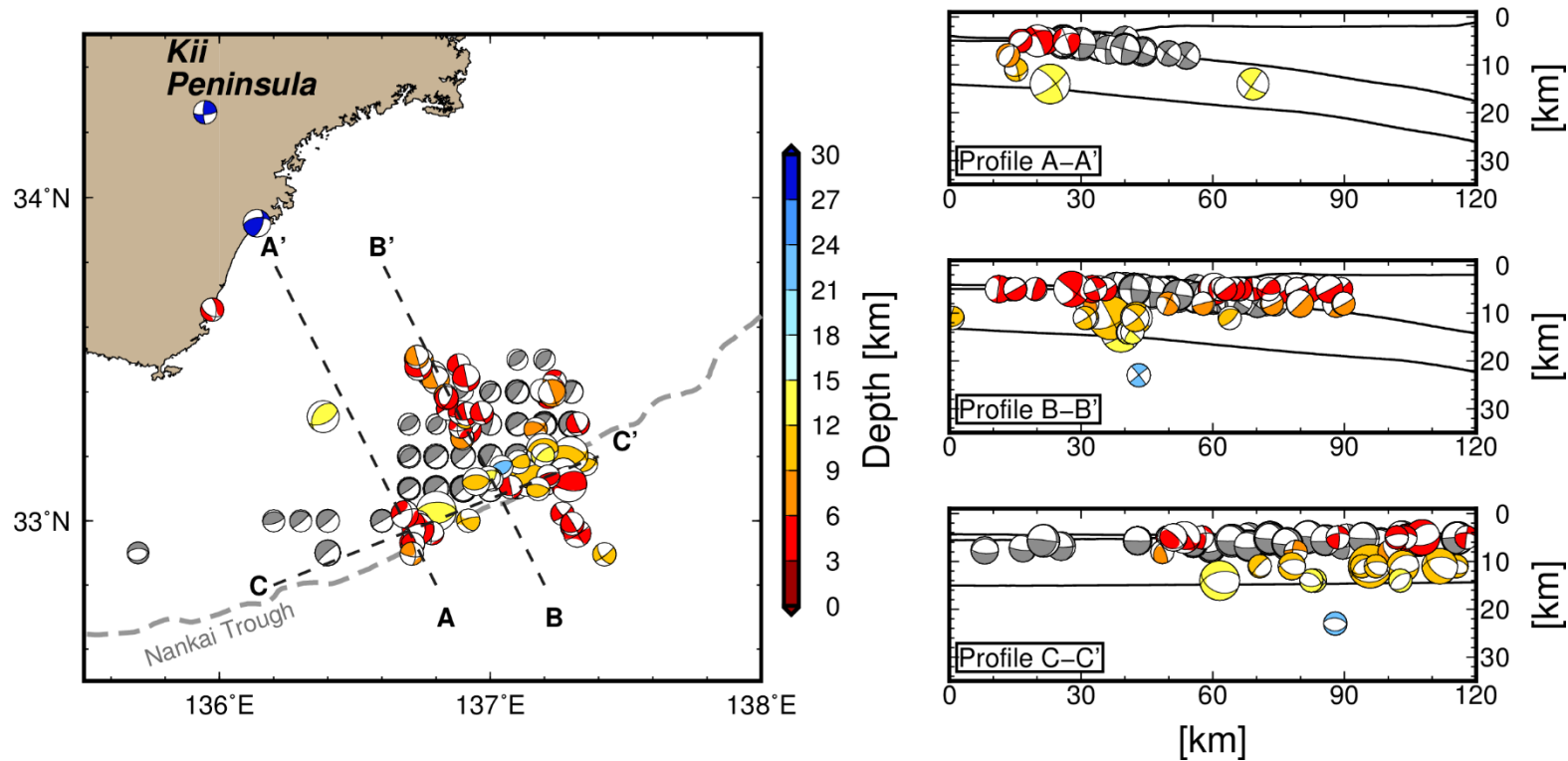


Figure S4. Spatial distribution of F-net MT solutions southeast of the Kii Peninsula. Coloured focal mechanisms are referenced from the F-net MT catalogue. Grey focal mechanisms are the CMT solutions of shallow VLFs (Takemura, Matsuzawa et al., 2019). Right-hand panels show cross-sections along profiles of A, B and C. The bathymetry of ETOPO1 (Amante & Eakins, 2009), the upper surface, and the oceanic Moho of the Philippine Sea Plate (Koketsu et al., 2012) along each profile are plotted in the right-hand panels.

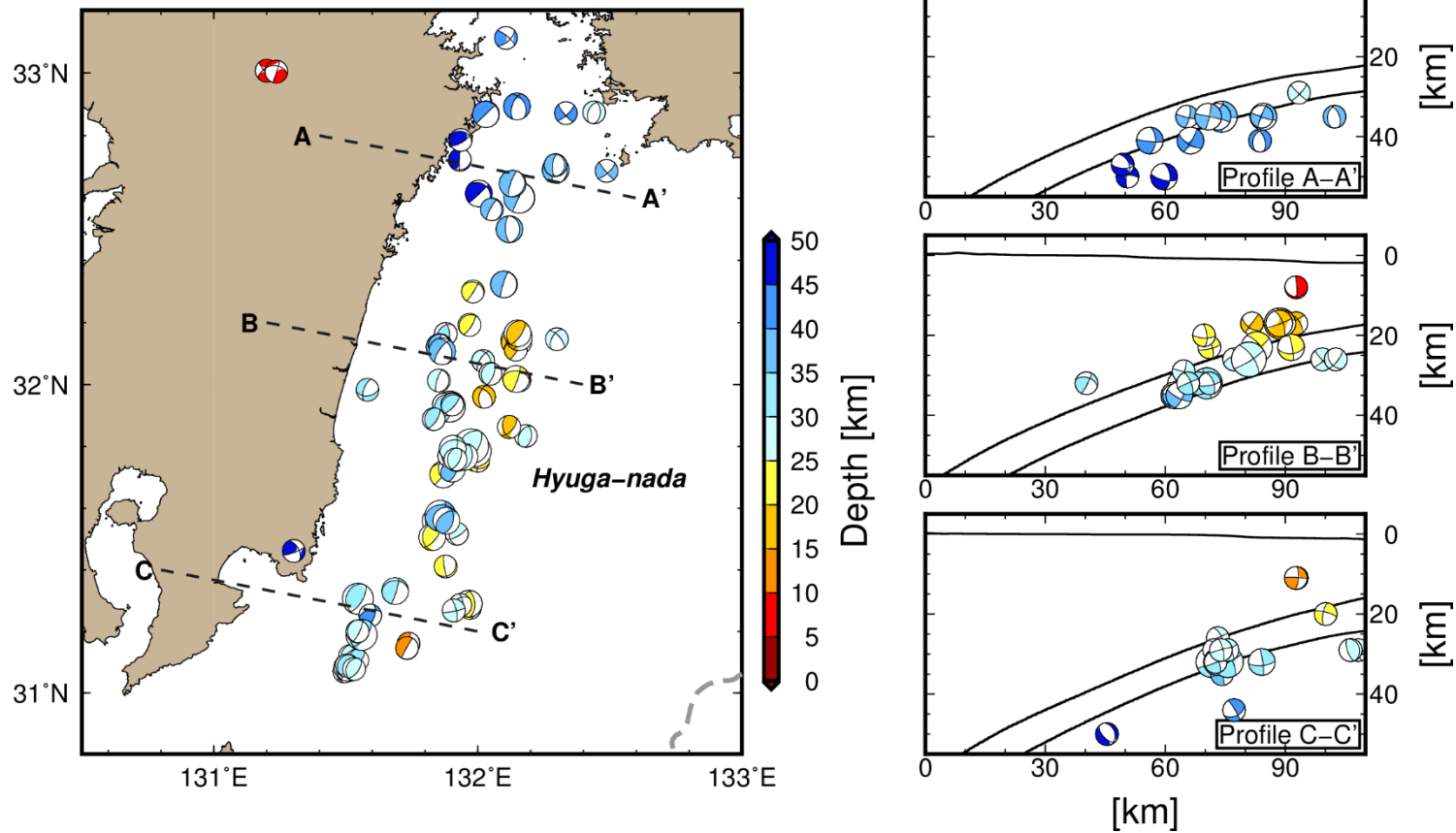


Figure S5. Spatial distribution of F-net MT solutions southeast of the Hyuga-nada region. Right-hand panels show cross-sections along profiles of A, B and C. The bathymetry of ETOPO1 (Amante & Eakins, 2009), the upper surface, and the oceanic Moho of the Philippine Sea Plate (Koketsu et al., 2012) along each profile are plotted in the right-hand panels.

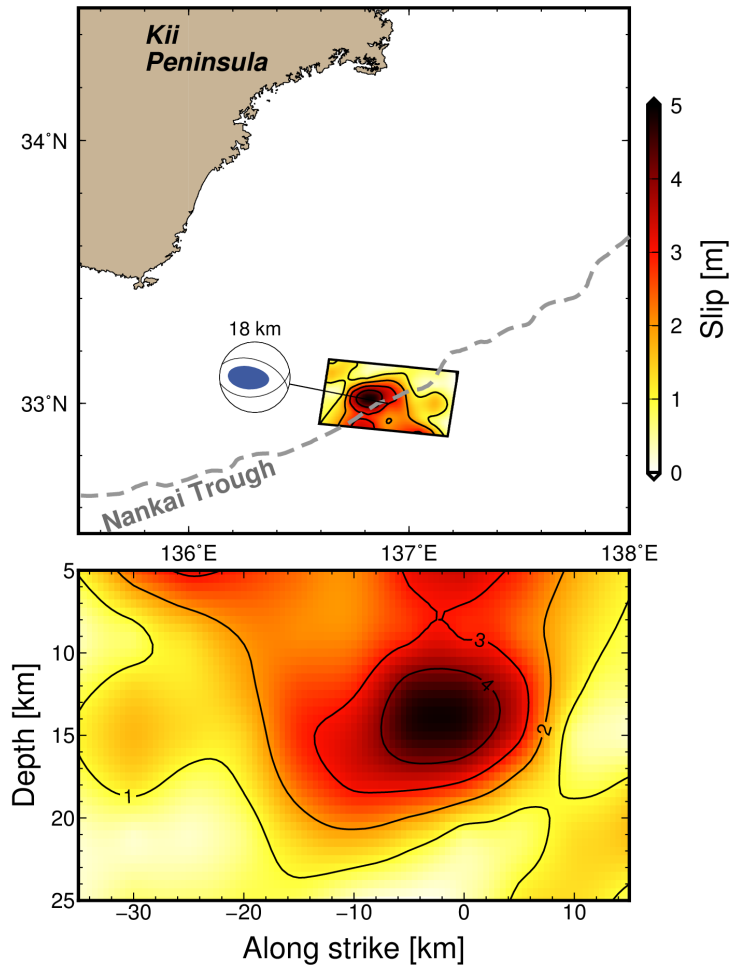


Figure S6. Comparison of the CMT results for the simulated M_w 7.2 southeast off the Kii Peninsula earthquake using the finite fault modelling (Okuwaki & Yagi 2018) solutions. In this CMT inversion, simulated seismograms using the finite fault modelling (Okuwaki & Yagi 2018) solution were used as observed seismograms. The bottom panel is the slip distribution of the finite fault model in the strike-depth plane.

Table S1. CMT solutions for all analysed moderate earthquakes.

Centroid time (UTC)	Lon.	Lat.	Depth [km]	M_{rr}	$M_{\theta\theta}$	$M_{\phi\phi}$	$M_{r\theta}$	$M_{r\phi}$	$M_{\theta\phi}$	Exp.	Mw	VR [%]
2004-04-21T07:26:30	132.3	33.5	38	-1.5100	-1.8500	2.9000	-2.4800	-1.2300	1.3700	22	4.34	67.45
2004-04-21T21:10:41	131.8	31.6	20	0.9760	0.2520	-0.3590	0.5200	0.6680	-0.2540	23	4.64	68.22
2004-04-21T21:20:52	131.8	31.5	24	1.9100	0.5570	-1.1000	0.7080	1.1300	-0.8800	23	4.84	78.46
2004-09-06T14:31:02	136.8	33.4	12	0.6040	-0.8920	1.5300	0.5790	0.5210	2.1800	24	5.55	82.86
2004-09-06T16:48:42	137.1	33.1	20	8.9900	-7.9500	0.5620	-0.1920	-2.1800	-2.2800	22	4.57	35.87
2004-09-06T17:59:37	136.9	33.5	14	0.0678	-0.5330	0.4660	0.0528	0.2790	0.9020	23	4.62	71.96
2004-09-06T20:06:48	137.1	33.6	8	1.5300	3.1600	-1.0500	2.1700	1.7800	-0.2500	22	4.32	65.56
2004-09-06T20:45:39	137.2	33.0	10	-0.3520	-2.4200	1.0300	-1.0300	-0.1840	1.0200	22	4.18	34.71
2004-09-06T22:49:05	136.8	33.4	14	-0.1690	-0.7280	0.9130	-0.4740	0.9630	0.8910	22	4.07	46.53
2004-09-06T22:59:28	136.8	33.5	12	0.5830	-2.8800	4.0400	-0.5310	1.2600	3.9300	22	4.42	77.34
2004-09-06T23:28:52	136.8	33.5	14	0.9900	-2.3300	3.3500	-1.0300	1.7300	2.6700	22	4.37	61.55
2004-09-07T00:35:45	137.0	33.1	8	0.7790	-2.0700	2.3900	-0.3200	3.3300	3.4900	22	4.42	66.03
2004-09-07T00:46:48	136.8	33.5	14	1.3300	-3.6700	5.5700	-1.6400	3.1700	4.4600	22	4.52	74.39
2004-09-07T00:54:35	136.7	33.5	16	-0.1140	-7.2000	6.7400	-1.2300	2.3000	6.3300	22	4.59	80.49
2004-09-07T01:10:05	136.8	33.4	14	0.5490	-3.1200	3.9500	-2.0500	3.9300	3.2200	22	4.48	77.42
2004-09-07T02:20:32	137.3	33.2	24	5.9200	-6.1500	0.2230	-1.5100	0.6320	-1.4300	22	4.47	76.12
2004-09-07T03:11:57	136.9	33.0	16	0.8740	-0.9970	0.2930	-0.7250	-0.0274	0.7540	23	4.70	78.61
2004-09-07T04:29:18	137.1	33.2	24	4.9000	-10.1000	0.6640	1.9100	-0.0017	-0.7360	22	4.54	68.2
2004-09-07T04:39:47	137.2	33.1	12	0.8410	-6.4300	2.4600	-0.1140	3.1000	0.3390	22	4.44	81.55
2004-09-07T04:59:32	136.6	32.9	8	0.7040	-1.2800	1.3200	1.2200	-0.9690	2.5300	22	4.28	59.12
2004-09-07T10:45:29	136.7	33.5	14	-0.0107	-0.7450	0.9020	-0.1830	0.3450	0.6880	23	4.64	78.17

2004-09-07T11:23:37	136.7	32.9	6	0.8930	0.5190	0.5580	4.0400	7.3800	3.1600	22	4.57	56.97
2004-09-07T14:02:48	136.7	33.5	16	-0.0584	-0.6920	0.8610	-0.2420	0.1940	1.2300	22	4.05	59.38
2004-09-07T17:29:41	137.3	33.2	24	4.3300	-11.2000	-0.4320	-1.4100	1.4000	-0.0673	25	6.56	81.44
2004-09-08T00:10:04	137.2	33.2	16	2.3000	-3.5800	-1.0400	-2.2200	-0.1920	-0.9520	23	5.00	82.86
2004-09-08T00:17:50	137.1	33.7	10	1.1100	2.1200	-1.0100	0.9700	0.8070	0.5910	22	4.17	51.85
2004-09-08T04:58:53	137.2	33.3	10	0.9130	-2.9700	5.0100	-0.3630	4.9100	3.5000	22	4.51	63.08
2004-09-08T05:56:30	137.0	33.4	12	-0.2580	-0.0829	3.1500	-1.0700	-2.4800	1.6200	22	4.32	42.47
2004-09-08T11:20:24	136.9	32.7	6	0.3250	-2.3400	2.6100	-1.2600	-2.5700	1.8700	22	4.35	67.83
2004-09-08T12:36:23	137.1	33.3	22	2.3700	-2.9700	-0.1930	0.9000	-0.2030	-0.1730	24	5.57	85.05
2004-09-08T15:02:14	137.1	33.6	8	1.2300	1.2300	-0.2840	1.6900	0.7740	0.0002	22	4.17	57.56
2004-09-09T08:40:10	137.2	33.0	8	0.1450	-1.4000	0.9040	-0.4990	0.2190	0.5310	24	5.36	85.86
2004-09-09T08:58:27	137.2	33.2	12	1.1200	-2.3800	0.2500	-0.3270	-0.3450	-0.2470	25	6.13	89.29
2004-09-10T20:05:57	136.6	33.0	10	0.0795	-0.4280	0.5350	0.4930	0.9040	2.1700	24	5.53	86.87
2004-09-12T03:05:58	136.7	32.9	10	0.2740	-1.3400	1.6600	-0.5860	2.0400	1.9200	22	4.27	83.36
2004-09-17T12:56:28	136.6	32.9	10	-0.5720	-0.4840	1.1900	2.8500	3.2900	4.2700	22	4.46	87.03
2004-09-18T18:48:38	136.8	33.5	12	0.1220	-0.6940	1.9900	0.1600	0.4740	2.5600	22	4.25	77.3
2004-09-20T14:17:51	137.2	33.6	8	0.4310	2.9600	-4.2100	2.2000	-0.4970	-1.3700	22	4.37	74.09
2004-09-28T09:37:43	137.3	33.0	10	0.4440	-1.9900	1.1600	-2.1800	1.1900	1.3100	22	4.28	83
2004-10-03T17:00:20	136.8	33.4	12	-0.2920	0.5230	3.2200	0.4630	0.2370	0.1240	22	4.18	71.88
2004-10-17T16:05:41	137.2	33.2	22	3.7600	-5.3300	1.0000	-1.2900	-2.6500	-1.9000	22	4.44	82.04
2004-10-28T06:27:30	135.2	33.6	34	-0.3740	-1.6700	2.2300	0.0469	-0.4460	-0.8680	22	4.16	69.66
2004-11-09T09:07:27	138.4	33.8	16	1.2800	-3.5400	-0.4050	-1.0100	0.6480	0.3660	24	5.58	82.93
2004-11-19T14:46:27	137.1	33.2	12	1.5700	-4.6800	-0.8920	-0.7280	-0.4220	-0.4780	22	4.31	80.91
2005-01-06T08:49:12	139.3	34.2	8	2.6600	-1.8000	3.3200	0.0929	0.5320	0.6500	22	4.29	53.42

2005-03-01T15:59:45	136.9	33.4	12	3.8000	-3.0200	7.6100	3.1300	1.8900	6.0700	22	4.59	84.06
2005-03-05T23:58:49	131.2	31.4	42	1.2400	-1.6700	1.4600	0.8400	1.2300	2.0300	22	4.26	64.99
2005-03-15T04:49:31	137.0	33.1	28	5.8700	-4.6000	-0.8160	-2.4000	-0.0550	-2.0400	22	4.46	82.27
2005-03-19T20:34:09	137.2	33.0	24	2.4000	-4.1300	0.0492	-0.3670	0.0348	-0.3640	22	4.29	64.7
2005-04-01T18:41:48	131.4	31.0	32	3.0500	-0.1300	-0.8730	1.1700	1.8200	-1.0400	22	4.28	68.09
2005-05-12T13:22:50	132.0	32.1	28	-0.6250	-0.0351	3.6100	1.3700	1.5400	0.5930	22	4.28	82.71
2005-05-26T05:31:29	132.3	33.4	46	-3.2300	-4.4200	7.2800	3.3400	2.2300	-1.7300	22	4.53	85.27
2005-05-27T12:17:18	133.7	34.0	36	-0.3810	-0.4810	1.0700	-0.4680	-0.3470	0.0844	23	4.61	89.65
2005-05-31T20:04:14	131.5	31.3	30	1.6900	0.7830	-0.3400	0.9510	0.8890	-0.3210	24	5.45	81
2005-11-01T21:47:34	135.1	33.8	46	-0.9580	0.6550	0.6100	-2.2700	-1.4100	1.1500	22	4.26	78.44
2005-12-03T19:39:01	137.0	33.1	26	8.7900	-8.7000	-4.0800	0.1430	0.8020	-3.3100	22	4.59	77.63
2005-12-03T20:01:21	137.0	33.1	28	4.3900	-7.3300	-4.8500	1.1900	1.4600	-4.1800	22	4.55	73.32
2005-12-11T03:32:08	132.0	32.0	26	1.5500	0.0063	-1.2300	1.2500	1.4500	-0.4200	22	4.19	76.16
2006-01-25T06:36:46	131.7	31.4	20	1.9700	-0.0443	-0.3050	1.0000	1.6100	-0.7570	22	4.20	67.21
2006-03-27T20:50:25	132.2	32.6	34	0.5430	0.3400	0.7660	0.6620	1.1100	-0.0280	24	5.38	86.62
2006-05-15T10:42:10	135.2	34.2	6	0.7870	0.3760	-3.2700	-0.0809	0.6340	-0.7800	22	4.21	86.19
2006-07-10T02:48:05	139.4	34.3	14	1.2700	0.2770	1.6400	-0.0862	0.1950	-0.8850	23	4.76	40.87
2006-11-18T10:08:35	132.0	31.9	32	-1.9100	-1.7900	5.5000	2.4100	-0.5070	-1.1900	22	4.41	75.13
2006-11-26T00:39:44	132.1	32.0	10	4.2400	0.7990	0.0740	2.6200	3.5400	-0.3240	22	4.42	60.13
2006-11-25T12:28:49	131.6	32.0	42	-0.3890	2.3300	0.9110	-0.1350	1.8300	1.9100	22	4.27	79.22
2006-11-25T11:49:31	139.4	34.2	12	0.4630	0.9330	1.4500	-0.6150	0.1020	-0.9650	23	4.75	67.16
2006-11-25T12:42:10	139.3	34.2	12	-1.7800	4.1300	2.8200	1.4000	-0.4390	-3.8400	22	4.43	69
2007-02-26T05:41:21	136.9	33.1	22	1.4000	-1.4700	-0.0424	0.6020	-0.2340	-0.1850	23	4.73	85.6
2007-03-24T01:20:52	136.9	33.4	10	0.2360	-0.7510	1.2100	0.2090	0.6620	1.3500	22	4.11	76.6

2007-04-15T21:19:28	136.4	34.8	14	1.9000	-1.1000	-3.3000	0.5050	0.7610	1.2400	23	4.94	71.68
2007-04-16T03:34:44	136.4	34.8	12	1.6900	0.0968	-2.4300	0.8840	-0.5490	0.1330	22	4.18	77.15
2007-04-26T18:02:54	133.6	33.9	34	0.5410	-3.3800	3.2000	-0.3530	0.9470	0.6560	23	4.96	88.57
2007-06-07T08:42:48	131.5	33.3	10	0.1110	1.2900	-0.4550	0.0837	0.3930	-0.2780	23	4.62	87.28
2007-06-08T02:22:14	131.5	33.3	8	0.6900	7.2800	-1.1500	0.3940	2.2100	-1.7100	22	4.45	84.5
2007-06-08T05:50:38	131.5	33.3	8	-0.3410	7.7300	-1.9500	-0.8060	2.8100	-1.6300	22	4.48	85.79
2007-07-17T02:24:17	135.9	34.3	38	0.1960	0.6830	0.2060	0.1410	-0.7580	-3.9000	22	4.34	61.32
2007-07-21T02:15:24	139.4	34.8	12	1.9700	0.9580	-0.2440	-1.0400	-1.0800	-3.2600	22	4.33	71.52
2007-07-31T19:22:39	131.9	32.2	26	1.9500	0.6120	-1.1400	-0.2330	0.8090	-0.4540	22	4.12	70.23
2007-08-19T19:21:54	138.6	34.0	50	0.5570	3.9900	-0.2680	3.3500	-6.0000	-2.0200	22	4.52	31.48
2007-10-21T11:09:26	131.9	32.2	28	2.3700	-0.8360	-0.5320	2.1100	3.3000	-1.3300	22	4.37	76.79
2007-10-22T18:35:59	139.1	34.2	14	6.5700	-0.7260	6.6900	-1.5000	2.5700	0.6990	22	4.51	83.03
2007-11-30T05:17:47	131.9	32.7	44	0.8450	-0.0984	2.3800	0.5950	4.0000	1.1800	22	4.37	83.26
2007-12-23T11:49:05	131.6	31.2	26	0.7680	-0.0350	0.6130	0.2310	1.0000	-0.6550	23	4.70	69.39
2008-03-10T19:44:30	131.8	31.8	18	3.1300	0.0972	-0.2790	1.7700	2.7100	-0.8190	23	5.00	75.47
2008-04-23T03:07:19	131.4	31.0	28	0.3990	-1.4000	-0.4010	-1.2200	-1.0600	-1.7300	22	4.21	54.25
2008-04-23T03:26:10	131.5	31.0	24	1.0200	-0.4460	0.8440	-1.0300	-0.8560	-0.9920	22	4.13	62.9
2009-04-06T03:36:27	131.9	31.9	26	1.6000	0.3630	-0.2710	0.9720	1.2800	-0.3600	24	5.47	78.17
2009-04-06T03:53:17	131.8	31.9	28	1.3600	0.3350	0.5540	0.9970	1.3700	0.4610	22	4.14	37.31
2009-05-26T05:26:20	137.8	34.7	28	0.4350	-4.6400	4.5700	-0.1080	1.6200	0.7650	22	4.40	82.58
2009-06-15T04:17:53	132.1	33.1	50	1.0400	-1.9200	3.5000	-0.3130	1.8300	0.0194	22	4.29	78.16
2009-06-20T13:22:17	135.0	32.9	6	0.9780	-0.4630	-0.0802	1.8300	0.9460	-0.3280	22	4.16	76.56
2009-07-23T08:51:00	134.3	33.0	16	2.0000	-2.1600	-1.5300	3.9200	5.1600	-1.5800	22	4.50	77.36
2009-07-28T14:30:54	131.8	32.0	32	0.3260	1.3800	2.5300	0.8300	1.4600	0.5420	22	4.22	77.51

2009-08-05T21:51:13	132.1	32.6	34	-0.6180	0.4690	2.1400	0.0996	1.1400	0.0227	23	4.80	85.05
2009-08-11T14:07:08	138.4	34.8	22	2.3400	-1.9500	0.5600	1.0700	0.7670	0.9580	25	6.22	79.55
2009-10-29T11:37:08	132.0	32.4	32	0.3630	4.3700	8.6200	2.2600	5.8200	0.9270	22	4.58	80.96
2009-12-16T23:12:50	133.4	33.2	30	0.7220	-3.7400	4.2200	-2.6800	-0.1910	-0.0985	22	4.39	69.81
2010-02-05T02:41:58	131.5	31.5	10	-2.2300	-0.2730	-0.3570	-0.9350	-1.8500	0.0247	22	4.21	61.72
2010-02-05T05:30:08	131.5	31.5	8	-0.7890	-0.1860	-0.3460	-0.5180	-1.2800	0.0114	23	4.72	65.27
2010-02-05T05:35:21	131.5	31.1	28	-0.5990	-0.2270	-1.4200	-0.5510	-1.7100	-0.9070	22	4.17	33.1
2010-03-05T15:49:55	139.5	33.8	16	-0.1790	-2.5100	3.7300	0.6980	-0.0789	-2.2300	22	4.33	69.12
2010-04-17T14:34:55	132.5	33.6	40	-2.3500	0.7910	2.2700	1.3300	-0.9060	-1.1100	22	4.26	84.9
2010-04-18T06:24:06	132.4	32.9	32	-2.1800	0.6880	3.2000	0.4310	-0.2830	0.8580	22	4.25	51.64
2011-01-17T05:33:22	133.8	34.0	36	-0.1260	-3.5100	3.7600	-0.6940	0.9810	4.8400	22	4.46	78.87
2011-02-01T11:32:24	132.0	31.7	22	0.8540	-0.3790	-0.5040	0.2120	0.5490	-0.6000	22	3.97	62.9
2011-02-05T03:11:23	131.5	31.0	32	2.7500	0.1790	-1.0300	0.9620	0.8370	-0.6420	23	4.87	68.85
2011-02-28T18:04:33	131.8	32.1	34	-0.4780	0.4270	2.0200	0.7020	0.9010	0.3580	23	4.79	78.53
2011-03-13T07:11:01	136.8	33.0	10	0.5130	-0.8780	6.0500	3.2200	1.0900	8.0300	22	4.59	52.28
2011-07-06T04:18:41	135.2	34.0	8	2.8800	-0.1930	-1.9900	-0.0750	1.2100	-1.4300	23	4.93	86.46
2011-07-06T04:34:53	135.2	34.0	8	2.2300	-0.3010	-1.8600	0.1840	1.1000	-1.1500	22	4.21	75.28
2011-07-25T08:32:11	136.1	34.0	38	1.2500	-0.6200	-0.0724	-0.4360	0.8300	-1.3200	23	4.79	78.51
2011-08-02T08:58:12	138.5	34.7	18	8.7200	-8.3200	-0.4010	4.6400	0.4010	0.2340	24	5.93	81.6
2011-08-12T13:37:45	138	34.4	10	1.7300	-0.5450	-1.1900	1.0100	1.5400	-0.7180	23	4.87	76.42
2011-08-28T18:52:02	131.2	31.0	30	5.5100	-0.3220	0.3930	1.8000	3.4000	-1.3800	22	4.44	70.95
2011-10-11T04:19:27	134.1	34.0	38	-1.8000	-0.9610	3.3900	-2.5100	1.3900	-0.4370	22	4.34	55.4
2012-01-30T12:18:20	132.0	32.6	44	0.6040	-0.4710	1.1500	2.0800	1.8100	-0.2870	23	4.91	84.49
2012-02-09T21:55:14	131.6	31.3	24	1.5200	-0.1100	0.0839	0.5160	1.1200	-0.6240	23	4.76	77.61

2012-02-29T10:23:01	131.9	31.8	18	0.9930	0.2130	-0.2410	0.5610	0.6860	-0.2020	23	4.65	70.72
2012-03-01T04:33:32	131.8	31.6	18	1.6200	0.6990	-0.7530	1.1600	2.8400	0.0018	22	4.28	72.98
2012-05-14T21:36:43	131.7	31.6	24	1.2300	-0.2870	0.0972	0.5740	0.9540	-0.5520	23	4.72	82.78
2012-06-20T12:35:32	132.3	32.1	30	-1.6900	-1.1000	3.3300	1.7200	-0.7720	-0.2970	22	4.28	68.9
2012-10-10T14:49:33	132.5	32.7	26	-0.1940	-4.5100	4.0800	-0.5900	0.4700	0.8570	22	4.37	80.93
2012-10-26T10:54:13	131.9	31.9	28	6.9100	-0.5030	-2.2800	3.7600	3.0000	-2.4500	22	4.52	74.92
2012-10-27T13:44:35	133.5	33.5	32	0.2950	-2.8700	3.2900	2.0400	-0.4650	-0.1490	22	4.32	78.78
2012-12-23T00:15:28	132.3	33.6	44	-2.2800	1.1800	3.8100	0.0741	1.6400	-0.4460	22	4.31	74.72
2013-03-12T03:34:51	131.8	31.6	22	1.0500	0.2970	-0.4430	0.5970	0.7460	-0.2560	24	5.34	74.59
2013-03-12T03:59:44	131.8	31.6	18	1.5200	0.3480	-0.3950	0.8020	0.9360	-0.2940	23	4.75	68.12
2013-04-13T14:33:17	134.8	34.4	14	3.2300	-0.0934	-4.0200	0.1170	-1.9900	0.7870	24	5.68	86.62
2013-04-17T19:15:22	139.4	34.1	12	3.3400	0.5930	-5.9100	-3.6200	0.7030	-4.9700	22	4.53	26.36
2013-04-17T20:13:57	139.5	34.0	6	2.5100	4.8900	-1.6900	1.3000	-0.0078	-6.0300	22	4.51	62.63
2013-04-17T20:16:18	139.4	34.1	10	-1.5600	3.7900	-2.3900	-1.1400	-1.6500	-4.9700	22	4.47	32.05
2013-04-17T21:22:12	139.4	34.1	10	0.0273	0.8930	-0.6150	-0.3640	-0.2790	-0.9960	23	4.68	75.46
2013-04-18T02:57:36	139.4	34.0	8	0.9590	-1.0200	2.1000	-0.2260	-2.0000	-4.3200	24	5.74	78.29
2013-06-10T19:11:01	139.4	33.2	10	1.8000	0.4650	1.0300	-1.5100	0.7290	0.1010	22	4.17	41.52
2013-08-03T18:56:13	137.5	34.6	32	-1.4300	0.9170	1.7500	-0.2710	-0.2480	0.7870	23	4.79	78.63
2013-08-18T17:00:59	139.4	33.3	12	0.1380	0.1800	0.4230	-0.1540	0.4480	-1.2100	23	4.69	74.86
2013-08-31T02:32:24	135.9	33.7	8	-1.4700	0.3350	2.0900	-0.1970	-0.5020	-1.8300	22	4.21	76.14
2013-09-28T13:37:47	131.5	31.2	28	1.7700	-0.7440	0.0424	0.1470	1.0500	-0.7720	22	4.12	58.21
2013-10-09T05:45:21	131.9	31.8	20	4.5900	0.5480	-1.4400	3.0400	3.6200	-1.4600	22	4.45	62.64
2013-12-12T20:25:13	131.2	31.2	30	-2.0100	0.9670	2.8600	-2.6700	-3.8600	-0.0001	22	4.42	48.1
2013-12-29T19:17:49	139.5	33.3	50	-0.8930	1.2000	3.9800	-3.3700	1.6700	-6.9600	22	4.55	48.6

2014-03-13T16:35:53	131.4	31.0	26	4.0700	0.1290	-1.5800	1.0800	0.8840	-1.5900	22	4.32	63.2
2014-04-04T09:46:42	132.1	32.5	34	0.6020	2.1100	3.9100	1.7600	2.7200	0.7310	22	4.37	74.38
2014-05-29T18:17:59	139.4	33.3	14	-5.2900	3.4200	3.5200	1.5200	-0.5440	-3.0200	22	4.46	72.95
2014-08-29T13:14:35	132.1	32.1	22	2.7700	-1.0100	-0.6080	2.3900	4.5000	-1.8200	24	5.78	82.64
2014-08-29T13:32:03	132.1	32.1	22	3.0400	-0.5990	-0.9730	4.1700	5.2600	-1.7000	22	4.51	45.04
2015-01-02T10:14:06	131.9	32.1	32	0.7340	1.1600	1.9300	0.4440	2.4600	0.1780	22	4.25	79.54
2015-01-31T01:45:54	131.8	31.8	18	4.8100	1.2500	-1.4400	2.9100	3.5800	-0.6980	22	4.45	64
2015-02-06T19:25:10	134.4	33.8	10	0.1400	0.9420	-0.9130	-0.1330	0.2550	-0.4570	23	4.62	85.96
2015-04-19T03:34:54	132.1	32.0	16	0.6220	-0.0366	-0.1890	0.5430	0.7160	-0.1400	23	4.61	70.71
2015-05-20T00:13:18	139.4	34.4	14	1.3100	1.0700	2.6300	-0.0486	0.0517	-4.1800	22	4.38	70.38
2015-05-26T10:35:21	131.9	31.8	22	2.5200	0.0556	-1.5400	1.5700	1.5700	-0.6770	22	4.26	65.76
2015-06-07T01:28:12	139.3	33.0	10	-1.9700	-0.5750	2.1800	0.7020	2.7700	-4.5800	22	4.44	69
2015-07-14T00:52:34	131.8	31.4	28	-1.8300	-0.5050	4.9800	-0.2720	4.7100	1.8100	22	4.47	42.29
2015-07-16T01:18:46	139.2	33.2	12	2.7700	0.3240	4.2400	-2.7500	3.6600	-0.3660	22	4.44	44.73
2015-07-19T11:13:42	131.3	31.3	20	-1.3000	-0.0173	0.6100	-0.8220	-0.9840	0.1300	23	4.74	67.6
2015-07-25T02:53:33	132.4	33.4	40	-4.5800	1.2200	7.4000	0.3360	4.3800	-0.2900	22	4.52	86.6
2015-08-22T01:54:34	132.2	33.3	44	-2.5300	1.6200	4.2100	1.6500	2.2500	1.1500	22	4.38	81.54
2015-08-26T16:51:35	131.9	32.1	34	-1.3000	-0.4380	3.9000	2.4100	1.4700	1.3700	23	5.02	82.74
2015-09-03T01:07:46	134.6	33.3	12	-2.8600	1.7300	1.2900	-0.5470	1.9300	-1.7600	22	4.31	76.71
2015-09-09T05:22:38	138.4	34.7	18	1.2900	-0.4620	0.3680	1.2300	2.2300	4.1400	22	4.40	81.52
2015-12-25T20:20:35	134.5	33.5	32	0.0457	-2.4100	2.6200	-0.6620	0.5150	0.1980	22	4.22	77.08
2016-04-01T20:39:08	136.4	33.4	10	3.7900	-1.4100	-0.6440	5.7600	7.4300	-1.5500	24	5.93	80.84
2016-04-16T16:11:36	131.4	33.3	6	1.5300	4.1900	-1.1700	1.5600	1.1500	-1.4700	23	5.01	83.35
2016-04-16T23:03:55	131.2	33.0	6	0.8010	3.7800	-3.2200	0.3090	1.3600	-1.0300	22	4.33	70.96

2016-04-22T08:20:36	134.3	33.5	30	-0.2900	-3.1100	4.2500	0.4440	0.2300	-0.3540	22	4.32	76.54
2016-04-30T00:09:33	131.4	33.3	6	0.4920	3.7800	-2.2400	1.0300	0.4920	-1.0100	22	4.29	63.2
2016-05-17T02:50:19	131.8	31.8	18	1.7900	0.2350	-0.2700	1.0200	1.3700	-0.3590	23	4.82	73.74
2016-07-12T00:22:00	139.4	33.3	14	-0.5700	1.7900	2.4600	0.6470	0.9710	-1.1000	23	4.89	80.29
2016-07-12T01:58:33	139.4	33.3	14	-2.9800	2.9000	3.2300	1.9700	1.2100	-1.9900	22	4.39	76.06
2016-07-12T02:33:01	139.5	33.2	10	-2.3100	2.5100	2.1900	1.7600	1.0200	-1.7900	22	4.33	58.82
2016-07-12T02:39:39	139.4	33.3	14	-0.5620	2.1100	2.6900	1.2300	0.6250	-1.4000	22	4.26	61.52
2016-07-12T04:31:10	139.4	33.3	14	-1.7100	1.9700	2.7800	1.0100	0.9590	-1.3800	22	4.28	70.48
2016-07-12T14:54:19	139.5	33.3	14	-1.2000	0.3680	0.7810	0.4930	-0.1700	-0.6490	23	4.68	80.11
2016-07-12T15:56:51	139.4	33.3	12	-3.5400	0.9930	3.5400	2.2700	-1.0900	-2.4300	22	4.40	73.1
2016-07-12T16:34:01	139.4	33.3	12	-2.5500	6.2000	5.5900	2.0900	2.5600	-4.3500	22	4.54	75.36
2016-07-13T15:24:51	139.5	33.2	12	-1.1500	2.8200	2.5200	1.0000	0.6950	-1.7300	22	4.30	57.3
2016-07-14T20:05:55	139.4	33.3	14	1.2900	2.5400	2.9600	0.8120	1.1500	-1.1000	22	4.29	20.44
2016-07-14T20:07:06	139.4	33.3	14	-1.0800	3.6400	4.3000	1.5800	1.4800	-2.2600	22	4.41	49.93
2016-07-14T20:17:26	139.4	33.3	12	-2.8500	3.1000	3.0200	1.4000	1.1700	-2.2100	23	5.05	80.29
2016-08-11T01:25:56	131.8	31.8	18	2.0200	0.0648	-0.0248	1.2900	1.9600	-0.4920	22	4.23	69.61
2016-10-22T12:33:44	131.9	32.8	50	3.7400	-4.4500	0.0375	4.7300	3.1400	-0.5440	22	4.50	83.13
2016-11-06T01:57:32	131.9	31.8	18	3.9600	0.6410	-0.3670	1.9800	2.6500	-0.6890	22	4.36	73.58
2016-11-19T20:48:00	135.4	33.9	48	-4.8700	-5.3000	6.4500	2.7200	-0.4450	-5.7800	23	5.25	87.65
2017-02-08T01:21:50	131.5	31.5	18	-1.4600	0.3990	-0.5350	-0.5660	-1.9700	0.0394	22	4.18	56.09
2017-02-08T12:19:26	134.6	33.4	32	0.0980	-2.2400	2.6200	-1.0400	0.3670	-0.7230	22	4.23	77.81
2017-03-03T08:53:42	132.1	32.7	34	-0.4610	2.3400	7.3400	1.5100	4.2700	0.7860	23	5.17	79.75
2017-06-17T07:39:50	131.8	31.9	26	4.4700	0.4820	-1.6800	2.9400	3.2200	-1.3000	22	4.44	80.08
2017-06-21T08:27:39	132.0	32.9	40	0.2360	0.5780	1.3100	1.2700	1.3700	0.6920	23	4.83	81.36

2017-07-02T09:58:21	131.3	33	10	-1.6700	1.9300	-1.3400	0.0344	-1.3000	2.6200	22	4.30	79.73
2017-09-20T03:33:07	132.3	33.4	40	-2.0300	0.9110	2.7200	0.0234	1.3100	-0.8110	22	4.24	78.71
2017-12-05T01:54:11	131.9	32.2	30	0.7080	-0.7160	1.0100	0.7960	1.6400	-0.2400	22	4.15	80.68
2018-01-09T14:51:52	131.8	33.2	40	-0.8680	-4.0500	-0.2880	1.4800	2.8800	-1.4000	22	4.37	29.96
2018-02-19T12:31:36	132.2	32.9	40	-2.4600	-0.1980	3.8100	1.7600	1.4800	-0.2860	23	5.00	84.71
2018-04-23T14:49:36	139.2	34.3	10	4.6400	1.4400	5.3800	0.9050	0.2380	-0.7390	22	4.41	77.28
2018-04-28T22:27:33	131.9	32.0	6	-4.4100	-1.9800	0.1830	-3.7800	-4.5300	0.0852	22	4.49	68.74
2018-06-12T13:54:20	131.5	31.1	30	2.0100	0.1340	-0.5320	0.6840	1.1400	-0.5430	24	5.48	74.03
2018-10-05T02:20:52	131.2	31.0	30	8.6400	-0.6640	0.1650	2.2500	4.7300	-2.2400	22	4.55	68.18
2018-11-03T01:53:53	135.2	33.7	40	-0.4100	0.0548	0.4150	0.2260	-0.6330	-0.8110	24	5.30	89.27
2018-11-05T17:19:13	135.3	33.7	46	-0.9130	-4.3300	4.4300	2.1900	-1.7500	-4.0400	22	4.48	81.7
2019-01-22T08:17:07	132.4	32.9	28	0.0827	-1.7100	1.7500	-0.2720	0.2710	0.3020	22	4.10	74.62
2019-03-12T00:37:48	132.7	33.2	34	-0.3650	-0.8620	1.0900	0.3180	0.2010	-0.5390	23	4.66	79.17
2019-03-13T22:48:46	134.9	33.8	38	0.2280	-6.3100	5.0700	-0.8290	-1.8600	-1.6400	23	5.13	84.24
2019-03-27T18:11:22	132.1	32.1	22	3.7800	-1.4500	-1.7600	3.2600	6.4300	-2.7900	23	5.21	83.68
2019-03-28T00:38:03	132.1	32.2	22	4.5800	-0.4790	-1.9300	4.6800	7.6100	-2.3900	23	5.26	84.47
2019-04-23T16:49:49	131.2	31.3	24	-1.8200	0.0989	0.5650	-1.2600	-2.2800	-0.0562	22	4.24	73.07
2019-05-10T16:43:23	131.9	31.8	20	3.2900	0.2030	-0.9640	2.1500	2.7900	-0.7340	24	5.69	73.07
2019-05-10T17:48:45	131.8	31.9	26	1.4000	0.1140	-0.5820	1.1400	1.5300	-0.4370	25	6.17	80.1
2019-05-10T18:07:36	131.9	31.8	26	2.5400	0.4640	-1.4000	0.9410	0.9770	-0.1030	23	4.86	50.82
2019-05-10T22:53:52	131.9	31.8	22	2.7100	1.2700	-1.6300	2.0200	1.1000	-0.8500	22	4.29	47.78
2019-05-11T05:40:37	131.8	31.8	28	4.2100	-2.7500	-2.5600	2.6500	5.0600	-2.0400	22	4.51	77.56
2019-05-11T17:59:38	132.3	32.7	32	-0.2330	0.2990	1.4400	0.3300	1.3200	-0.1170	23	4.76	87.79
2019-05-13T00:07:41	132.3	32.7	32	-0.9350	0.6150	2.5100	0.2610	1.9400	-0.0225	22	4.23	77.08

2019-06-19T20:35:44	131.2	31	32	3.8600	-0.1390	0.3560	1.2000	2.9300	-0.7980	22	4.35	58.62
2019-07-27T11:11:46	131.8	31.6	24	2.7700	-0.5160	0.8590	1.4300	2.5800	-1.4700	22	4.33	80.01
2004-04-21T07:26:30	132.3	33.5	38	-1.5100	-1.8500	2.9000	-2.4800	-1.2300	1.3700	22	4.34	67.45

Table S2. CMT solutions for the M_w 7.2 and 7.5 earthquakes.

Centroid time (UTC)	Lon.	Lat.	Depth [km]	M_{rr}	$M_{\theta\theta}$	$M_{\phi\phi}$	$M_{r\theta}$	$M_{r\phi}$	$M_{\theta\phi}$	Exp.	Mw	VR [%]
2004-09-05T 10:07:12	136.7	33.1	26	0.4435	-7.6109	-2.2143	-0.331	0.4022	0.3545	26	7.10	71.76
2004-09-05T 14:57:43	137.0	33.2	20	0.6117	-1.3773	-0.0418	-0.3787	0.1300	0.1093	27	7.31	71.83